NASA/CR-2001-210836
ICASE Report No. 2001-6

High-order/Spectral Methods on Unstructured Grids I. Time-domain Solution of Maxwell's Equations

J.S. Hesthaven and T. Warburton
Brown University, Providence, Rhode Island

ICASE
NASA Langley Research Center
Hampton, Virginia

Operated by Universities Space Research Association

National Aeronautics and
Space Administration

Langley Research Center
Hampton, Virginia 23681-2199

Prepared for Langley Research Center
under Contract NAS1-97046

March 2001

Form SF298 Citation Data

Report Date *("DD MON YYYY")* 00MAR2001	**Report Type** N/A	**Dates Covered (from... to)** *("DD MON YYYY")*

Title and Subtitle High-order/Spectral Methods on Unstructured Grids I. Time-domain Solution of Maxwells Equations	**Contract or Grant Number**
	Program Element Number
Authors J.S. Hesthaven and T. Warburton	**Project Number**
	Task Number
	Work Unit Number
Performing Organization Name(s) and Address(es) National Aeronautics and Space Administration Langley Research Center Hampton, Virginia 23681-2199	**Performing Organization Number(s)**
Sponsoring/Monitoring Agency Name(s) and Address(es)	**Monitoring Agency Acronym**
	Monitoring Agency Report Number(s)

Distribution/Availability Statement
Approved for public release, distribution unlimited

Supplementary Notes
ICASE Report No. 2001-6

Abstract
Abstract. We present an ab initio development of a convergent high-order accurate scheme for the solution of linear conservation laws in geometrically complex domains. As our main example we present a detailed development and analysis of a scheme suitable for the time-domain solution of Maxwell's equations in a three-dimensional domain. The fully unstructured spatial discretization is made possible by the use of a high-order nodal basis, employing multivariate Lagrange polynomials de ned on the triangles and tetrahedra. Careful choices of the unstructured nodal grid points ensure high-order/spectral accuracy, while the equations themselves are satis ed in a discontinuous Galerkin form with the boundary conditions being enforced weakly through a penalty term. Accuracy, stability, and convergence of the semi-discrete approximation to Maxwell's equations is established rigorously and bounds on the global divergence error are provided. Concerns related to eÆcient implementations are discussed in detail. This sets the stage for the presentation of examples, verifying the theoretical results, as well as illustrating the versatility, exibility, and robustness when solving two- and three-dimensional benchmarks in computa- tional electromagnetics. Pure scattering as well as penetration is discussed and high parallel performance of the scheme is demonstrated.

Subject Terms

Document Classification unclassified	**Classification of SF298** unclassified
Classification of Abstract unclassified	**Limitation of Abstract** unlimited
Number of Pages 41	

HIGH-ORDER/SPECTRAL METHODS ON UNSTRUCTURED GRIDS I. TIME-DOMAIN SOLUTION OF MAXWELL'S EQUATIONS *

J.S. HESTHAVEN† AND T. WARBURTON‡

Abstract. We present an ab initio development of a convergent high-order accurate scheme for the solution of linear conservation laws in geometrically complex domains. As our main example we present a detailed development and analysis of a scheme suitable for the time-domain solution of Maxwell's equations in a three-dimensional domain. The fully unstructured spatial discretization is made possible by the use of a high-order nodal basis, employing multivariate Lagrange polynomials defined on the triangles and tetrahedra. Careful choices of the unstructured nodal grid points ensure high-order/spectral accuracy, while the equations themselves are satisfied in a discontinuous Galerkin form with the boundary conditions being enforced weakly through a penalty term. Accuracy, stability, and convergence of the semi-discrete approximation to Maxwell's equations is established rigorously and bounds on the global divergence error are provided. Concerns related to efficient implementations are discussed in detail.

This sets the stage for the presentation of examples, verifying the theoretical results, as well as illustrating the versatility, flexibility, and robustness when solving two- and three-dimensional benchmarks in computational electromagnetics. Pure scattering as well as penetration is discussed and high parallel performance of the scheme is demonstrated.

Subject classification. Applied Mathematics

Key words. high-order/spectral accuracy, stability, convergence, unstructured grids, Maxwell's equations

1. Introduction. The ability to accurately and reliably model wave-dominated problems continues to be an essential, and in many cases an enabling, technology in the development and analysis of emerging technologies such as stealth technology, noise reduction, subsurface exploration and optical communication to name a few. These are all problems characterized by being very large in terms of a characteristic wavelength, geometrically extremely complex, often composed of a heterogeneous collection of different materials and all requiring a high fidelity solution with a rigorous control of the numerical errors. Even for linear problems such conditions forces one to look beyond standard computational techniques and seek new computational frameworks enabling the accurate, efficient, and robust modeling of wave-phenomena over long times in settings of a realistic geometric complexity.

The requirement that one can accurately propagate waves over many periods of time naturally suggests that high-order/spectral methods be considered [1]. On the other hand, the use of such methods is traditionally in conflict with the need for significant geometric flexibility by being restricted to fairly simple geometries. The standard approach to overcome this restriction is to introduce a multi-element formulation

*This work was partially supported by AFOSR/DARPA under contract F49620-1-0426 and by the National Aeronautics and Space Administration under NASA Contract NAS1-97046 while the authors were in residence at ICASE, NASA Langley Research Center, Hampton, VA 23681-2199. JSH also acknowledge support by the Alfred P. Sloan Foundation as a Sloan Research Fellow.

†Division of Applied Mathematics, Brown University, Box F, Providence, RI 02912.
E-mail: *Jan.Hesthaven@brown.edu*

‡Division of Applied Mathematics, Brown University, Box F, Providence, RI 02912.
E-mail: *timw@cfm.brown.edu*

in which the basic building block is parametrically mapped cubes in the spirit of finite element methods. This approach has been very successfully applied to the solution of problems in fluid mechanics [2, 3, 4], gasdynamics [5, 6, 7, 8, 9, 10], and electromagnetics [11, 12, 13, 14, 15].

While such techniques, when applicable, are powerful they do suffer from the need to tile the computational using only hexahedral elements. Unfortunately, automated grid generation using only such elements for general three-dimensional computational problems of a realistic complexity remains a very nontrivial task and is typically very time-consuming. Furthermore, spatial adaptation, while certainly possible, is quite a challenge with a method based solely on hexahedral elements. On the other hand, automated grid generation employing a fully unstructured grid is significantly more mature, due mainly to extensive developments within the finite-element community. Spatial grid adaptation is also considerably easier within a fully unstructured grid formulation.

It is with these issues in mind that we present an ab initio development of a computational framework that combines the strengths of a high-order/spectral formulation with the flexibility of a fully unstructured grid. The formulation relies on the resolution of two central issues. On one hand we shall discuss in detail how to represent functions defined on triangles and tetrahedra to high accuracy and how this translates into the construction of basic operators needed to solve partial differential equations. On the other hand we need to address the issue of how to use such a high-order representation to formulate a convergent scheme suitable for solving systems of linear hyperbolic problems in general and Maxwell's equations in particular.

Much in the spirit of the original work on spectral element methods [2, 3] we shall focus on the formulation of efficient and flexible unstructured grid methods using nodal elements. This is in contrast to past attempts to develop high-order unstructured grid methods, suitable for solving time dependent problems, which have been focused on the use of high-order modal expansions, e.g., [16, 17, 18, 19, 20, 21]. In these works, modal expansions of orthogonal polynomials defined on the simplex are utilized while a straightforward monomial basis is used in [22] (see also [23] and references therein) much in the tradition of classical high-order finite element methods for elliptic problems [24, 25].

In contrast to the classical spectral element approach, however, we do not seek a globally continuous solution but rather require that the equations be satisfied in a discontinuous Galerkin/penalty fashion. This is related to the classic discontinuous Galerkin finite element method [23] although the present approach represents a more general formulation, containing the classic discontinuous Galerkin formulation as a special case. Such more general techniques have been known in the context of spectral methods as penalty methods [26] for a while and recently stable formulations on general one-dimensional [27], triangular [28], and tetrahedral domains [29] have been discussed. These methods all share the great advantage of a complete decoupling of all elements, hence enabling high parallel efficiency, and allows for discontinuous solutions between elements in a natural way. As we shall see later, this is essential in allowing for the inclusion of material interfaces in a natural and straightforward manner.

While the majority of what we shall discuss is of a very general nature we have chosen to discuss in detail the development and analysis of a high-order/spectral accuracy unstructured grid scheme for the solution of Maxwell's equations in the time-domain. This is not only a challenging problem but also a problem of significant contemporary interest due to emerging technologies such as broad-band target illumination and penetration, advanced materials and diffraction based modern optics, all characterized by being electrically large, having a significant separation of scales and requiring substantial geometric flexibility of the computational framework. On the other hand, Maxwell's equations serve as an excellent example of numerous other linear hyperbolic systems of equations in, e.g., elasticity, acoustics, solid mechanics etc, for which

the presented framework can be adapted with little effort. In part II of this work [30] we shall discuss in detail generalizations of the proposed computational framework with an emphasis on the solution of general systems of conservation laws.

What remains of the paper is organized as follows. In Sec. 2 we set the stage by briefly describing the physical setting, Maxwell's equations, their normalized and scattered field formulations, as well as boundary conditions at material interfaces and metallic boundaries. The first step in the construction of a high-order/spectral unstructured grid scheme for the solution of Maxwell's equations is taken in Sec. 3 where we introduce a Lagrangian high-order basis on the general curvilinear simplex. In the appendix we include a discussion of techniques allowing for efficient and accurate implementations of the basic operators, e.g., differentiation, filtering, and high-order integration in volumes and on faces. By providing the basic building block for the spatial approximation, this development sets the stage for the formulation of a high-order/spectral convergent scheme for solving Maxwell's equations as discussed in Sec. 4. The convergence of the scheme, being a generalized discontinuous Galerkin/penalty method, is established in the classic way through consistency as well as local and global stability. A stronger and optimal result is furthermore established by showing the scheme to be error-bounded, guaranteeing at most linear growth in time and control over the growth rate. This result is also used to establish bounds on the behavior of the divergence error. Verification and performance of the complete scheme is the topic of Sec. 5 where we present a number of simple tests, verifying the theoretical results, prior to illustrating the efficiency, versatility, and robustness of the computational framework for the solution of two- and three-dimensional scattering and penetration problems. We shall also briefly discuss measures taken in the implementation of the scheme to ensure efficient execution on large scale contemporary parallel computational platforms. In Sec. 6 we conclude by offering a few remarks and guidelines for future work within the present framework.

2. The Physical Setting and Maxwell's Equations. We shall concern ourselves with the direct solution of Maxwell's equations on differential form

$$\frac{\partial \tilde{\boldsymbol{D}}}{\partial \tilde{t}} = \tilde{\nabla} \times \tilde{\boldsymbol{H}} + \tilde{\boldsymbol{J}} \quad , \quad \frac{\partial \tilde{\boldsymbol{B}}}{\partial \tilde{t}} = -\tilde{\nabla} \times \tilde{\boldsymbol{E}} \ , \tag{1}$$

$$\tilde{\nabla} \cdot \tilde{\boldsymbol{D}} = \tilde{\rho} \ , \ \ \tilde{\nabla} \cdot \tilde{\boldsymbol{B}} = 0 \ , \tag{2}$$

within the general three-dimensional domain, Ω, with the charge distribution, $\tilde{\rho}(\tilde{\boldsymbol{x}}, \tilde{t})$. The electric field, $\tilde{\boldsymbol{E}}(\tilde{\boldsymbol{x}}, \tilde{t})$, and the electric flux density, $\tilde{\boldsymbol{D}}(\tilde{\boldsymbol{x}}, \tilde{t})$, as well as the magnetic field, $\tilde{\boldsymbol{H}}(\tilde{\boldsymbol{x}}, \tilde{t})$, and the magnetic flux density, $\tilde{\boldsymbol{B}}(\tilde{\boldsymbol{x}}, \tilde{t})$, are related through the constitutive relations

$$\tilde{\boldsymbol{D}} = \tilde{\varepsilon} \tilde{\boldsymbol{E}} \ , \ \ \tilde{\boldsymbol{B}} = \tilde{\mu} \tilde{\boldsymbol{H}} \ .$$

The permittivity tensor, $\tilde{\varepsilon}$, as well as the permeability tensor, $\tilde{\boldsymbol{\mu}}$, are in general anisotropic and may depend on space and time as well as the strength of the fields themselves. The current, $\tilde{\boldsymbol{J}}$, is typically assumed to be related to the electric field, $\tilde{\boldsymbol{E}}$, through Ohms law, $\tilde{\boldsymbol{J}} = \tilde{\sigma} \tilde{\boldsymbol{E}}$, where $\tilde{\sigma}$ measures the finite conductivity, although more complex relations are possible.

In this work, we shall restrict the attention to materials which can be assumed isotropic, linear and time-invariant, in which case the constitutive relations take the form

$$\tilde{\boldsymbol{D}} = \tilde{\varepsilon}_0 \varepsilon_r \tilde{\boldsymbol{E}} \ , \ \ \tilde{\boldsymbol{B}} = \tilde{\mu}_0 \mu_r \tilde{\boldsymbol{H}} \ .$$

Here $\tilde{\varepsilon}_0 = 8.854 \times 10^{-12}$ F/m and $\tilde{\mu}_0 = 4\pi \times 10^{-7}$ H/m represent the vacuum permittivity and permeability, respectively, and $\varepsilon_r(\boldsymbol{x})$ and $\mu_r(\boldsymbol{x})$ refers to the relative permittivity and permeability, respectively, of the materials.

Taking the divergence of Eq.(1) and applying Eq.(2) in combination with Gauss' law for charge conservation immediately confirms that if the initial conditions satisfy Eq.(2), and the fields are evolved according to Maxwell's equations, Eq.(1), the solution will satisfy Eq.(2) at all times. Hence, one can view Eq.(2) as a consistency condition on the initial conditions and limit the solution to the time-dependent part of Maxwell's equations, Eq.(1).

To simplify matters further, we shall consider the non-dimensionalized equations for which we introduce the normalized quantities

$$\boldsymbol{x} = \frac{\tilde{\boldsymbol{x}}}{\tilde{L}} \quad , \quad t = \frac{\tilde{t}}{\tilde{L}/\tilde{c}_0} \quad ,$$

where $\tilde{L}$ is a reference length, and $\tilde{c}_0 = (\tilde{\varepsilon}_0\tilde{\mu}_0)^{-1/2}$ represents the dimensional vacuum speed of light. The fields themselves are normalized as

$$\boldsymbol{E} = \frac{\tilde{Z}_0^{-1}\tilde{\boldsymbol{E}}}{\tilde{H}_0} \quad , \quad \boldsymbol{H} = \frac{\tilde{\boldsymbol{H}}}{\tilde{H}_0} \quad , \quad \boldsymbol{J} = \frac{\tilde{\boldsymbol{J}}\tilde{L}}{\tilde{H}_0} \quad ,$$

where $\tilde{Z}_0 = \sqrt{\tilde{\mu}_0/\tilde{\varepsilon}_0}$ refers to the dimensional free space intrinsic impedance, and $\tilde{H}_0$ is a dimensional reference magnetic field strength.

With this normalization Eq.(1) takes the nondimensional form

$$\varepsilon_r \frac{\partial \boldsymbol{E}}{\partial t} = \nabla \times \boldsymbol{H} + \boldsymbol{J} \quad , \quad \mu_r \frac{\partial \boldsymbol{H}}{\partial t} = -\nabla \times \boldsymbol{E} \quad , \tag{3}$$

which is the general form of the equations we consider in the following.

To solve Maxwell's equations in the vicinity of boundaries, penetrable or not, we shall need boundary conditions relating the field components on either side of the boundary.

Assuming that a normal unit vector, $\hat{\boldsymbol{n}}$, to the boundary is given, the boundary conditions on the electric field components take the form

$$\hat{\boldsymbol{n}} \times (\boldsymbol{E}_1 - \boldsymbol{E}_2) = 0 \quad , \quad \hat{\boldsymbol{n}} \cdot (\boldsymbol{D}_1 - \boldsymbol{D}_2) = \rho_s \quad ,$$

where $\boldsymbol{E}_i$ and $\boldsymbol{D}_i$, $i = (1, 2)$, represent the fields on either side of the interface and ρ_s represents a surface charge. Equivalently, the conditions on the magnetic fields are given as

$$\hat{\boldsymbol{n}} \times (\boldsymbol{H}_1 - \boldsymbol{H}_2) = \boldsymbol{J}_s \quad , \quad \hat{\boldsymbol{n}} \cdot (\boldsymbol{B}_1 - \boldsymbol{B}_2) = 0 \quad ,$$

where $\boldsymbol{J}_s$ represents a surface current density.

In the general case of materials with finite conductivity, no surface charges and currents can exist, and the simplified conditions take the form

$$\hat{\boldsymbol{n}} \times (\boldsymbol{E}_1 - \boldsymbol{E}_2) = 0 \quad , \quad \hat{\boldsymbol{n}} \times (\boldsymbol{H}_1 - \boldsymbol{H}_2) = 0 \quad , \tag{4}$$

expressing continuity of the tangential field components, while the normal components of the flux densities must satisfy

$$\hat{\boldsymbol{n}} \cdot (\boldsymbol{D}_1 - \boldsymbol{D}_2) = 0 \ , \ \ \hat{\boldsymbol{n}} \cdot (\boldsymbol{B}_1 - \boldsymbol{B}_2) = 0 \ , \tag{5}$$

i.e., they are likewise continuous, while the normal components of the fields themselves are discontinuous.

For the important special case of a perfect conductor, the conditions take a special form as the perfect conductor supports surface charges and currents while the fields are unable to penetrate into the body, i.e.,

$$\hat{\boldsymbol{n}} \times \boldsymbol{E} = 0 \ , \ \ \hat{\boldsymbol{n}} \cdot \boldsymbol{B} = 0 \ . \tag{6}$$

2.1. The Scattered Field Formulation. For scattering and penetration problems involving linear materials it is often advantageous to exploit the linearity of Maxwell's equations and solve for the scattered field, $(\boldsymbol{E}^{\mathrm{s}}, \boldsymbol{H}^s)$, rather than for the total field, $(\boldsymbol{E}, \boldsymbol{H})$, which are trivially related as

$$\boldsymbol{E} = \boldsymbol{E}^i + \boldsymbol{E}^s \ , \ \ \boldsymbol{H} = \boldsymbol{H}^i + \boldsymbol{H}^s \ ,$$

where $(\boldsymbol{E}^i, \boldsymbol{H}^i)$ represents the incident field, illuminating the scattering object. Assuming that $(\boldsymbol{E}^i, \boldsymbol{H}^i)$ represents a particular solution to Maxwell's equations, one recovers the scattered field formulation

$$\varepsilon_r \frac{\partial \boldsymbol{E}^s}{\partial t} = \nabla \times \boldsymbol{H}^s + \sigma \boldsymbol{E}^s - \left(\varepsilon_r - \varepsilon_r^i\right) \frac{\partial \boldsymbol{E}^i}{\partial t} + (\sigma - \sigma^i)\boldsymbol{E}^i \ , \tag{7}$$

$$\mu_r \frac{\partial \boldsymbol{H}^s}{\partial t} = -\nabla \times \boldsymbol{E}^s - \left(\mu_r - \mu_r^i\right) \frac{\partial \boldsymbol{H}^i}{\partial t} \ , \tag{8}$$

where $\varepsilon_r^i(\boldsymbol{x})$, $\mu_r^i(\boldsymbol{x})$, and $\sigma^i(\boldsymbol{x})$ refers to the relative permittivity, permeability and conductivity of the media in which the incident field represents a solution to Maxwell's equations. To simplify matters we have assumed Ohms law, $\boldsymbol{J} = \sigma \boldsymbol{E}$. We note that the important special case of a vacuum field illuminating the scattering object is recovered by using $\varepsilon_r^i = \mu_r^i = 1$, $\sigma^i = 0$, and using a free space solution in the forcing function.

In this formulation, the boundary conditions along a dielectric interface take the form

$$\hat{\boldsymbol{n}} \times (\boldsymbol{E}_1^s - \boldsymbol{E}_2^s) = 0 \ , \ \ \hat{\boldsymbol{n}} \times (\boldsymbol{H}_1^s - \boldsymbol{H}_2^s) = 0 \ , \tag{9}$$

for the tangential components, while the conditions on the scattered field components becomes

$$\hat{\boldsymbol{n}} \times \boldsymbol{E}^s = -\hat{\boldsymbol{n}} \times \boldsymbol{E}^i \ , \ \ \hat{\boldsymbol{n}} \cdot \boldsymbol{B}^s = -\mu_r \hat{\boldsymbol{n}} \cdot \boldsymbol{H}^i \ , \tag{10}$$

in the case of a perfectly conducting boundary. As we shall see shortly, there is no need to consider the conditions on the normal components further.

3. The Nodal Element. We shall seek approximate solutions to Maxwell's equations in a general domain, Ω, possibly containing a heterogeneous collection of scattering and penetrable bodies. To facilitate the required geometric flexibility, we represent the computational domain as the union of K non-overlapping body-conforming d-simplices, D. Hence, for two-dimensional problems we shall use triangles as the geometric building block while the tetrahedron is employed to fill the computational volume.

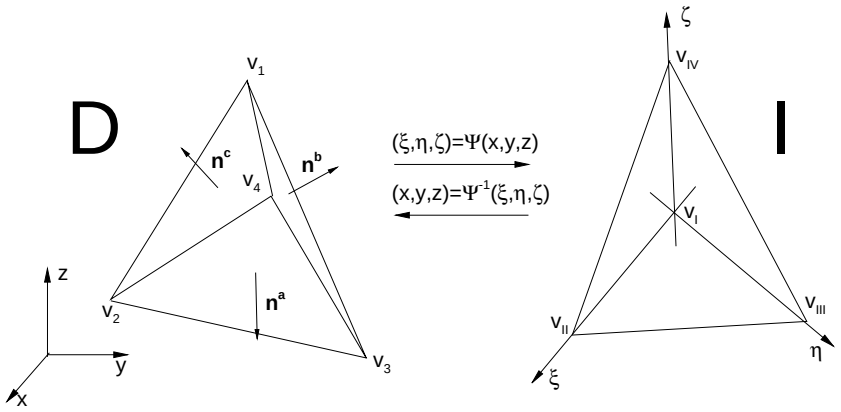

FIG. 1. *Mapping between the curvilinear tetrahedral,* D*, and the standard tetrahedral,* I*, including the numbering and notation employed in the text.*

While this multi element formulation is essential in enabling the solution of geometrically complex problems, it also introduces new complications, the understanding and resolution of which are at the heart of the construction of the scheme. In particular, the use of simplices requires an understanding of how to construct high-order accurate Lagrange interpolation polynomials on such elements and, subsequently, how we can formulate approximations to basic operations such as interpolation, differentiation and integration of functions defined on general curvilinear d-simplices. These are issues we shall deal with in the following. For continuity we shall postpone the discussion of practical, yet essential, techniques for the efficient and accurate implementation of the basic operations to the appendix.

The equally important question of how to exploit this knowledge to construct global high-order/spectral accuracy solution techniques suitable for Maxwell's equations as well as other linear hyperbolic systems is the central issue addressed in Section 4.

3.1. The Curvilinear d-Simplex. We start by assuming that the computational domain, Ω, is decomposed into curvilinear d-simplices, $\mathsf{D} \subset \mathsf{R}^d$, as illustrated in Fig. 1 by a 3-simplex, a tetrahedron. For generality we shall limit much of the discussions to the three-dimensional case and regard the two-dimensional problem as a natural simplification.

While we shall not require that the faces of the tetrahedron are planar, such an assumption will, as we shall see shortly, significantly simplify matters in terms of analysis as well as implementation. It should also be noted that for most computational problems, the vast majority of the elements will have planar faces which thus supplies the single most important special case.

Let us introduce the standard tetrahedron, $\mathsf{I} \subset \mathsf{R}^3$, given by the vertices

$$\boldsymbol{v}_{\mathrm{I}} = \begin{bmatrix} -1 \\ -1 \\ -1 \end{bmatrix} \quad , \quad \boldsymbol{v}_{\mathrm{II}} = \begin{bmatrix} 1 \\ -1 \\ -1 \end{bmatrix} \quad , \quad \boldsymbol{v}_{\mathrm{III}} = \begin{bmatrix} -1 \\ 1 \\ -1 \end{bmatrix} \quad , \quad \boldsymbol{v}_{\mathrm{IV}} = \begin{bmatrix} -1 \\ -1 \\ 1 \end{bmatrix} \quad ,$$

as illustrated in Fig. 1 with the corresponding vertices in D termed $\boldsymbol{v}_1$-$\boldsymbol{v}_4$. To fix the notation within the tetrahedron, let us also name the face in D opposite vertex $\boldsymbol{v}_1$, i.e, spanned by the three vertices $\boldsymbol{v}_2$, $\boldsymbol{v}_3$, and $\boldsymbol{v}_4$, for face 'a', that opposite of vertex $\boldsymbol{v}_2$ for face 'b' and so forth. In general we shall name the coordinates in the physical simplex, D, as $\boldsymbol{x} = (x, y, z)$ while the coordinates, $\boldsymbol{\xi} \in \mathsf{I}$, shall be referred to as $\boldsymbol{\xi} = (\xi, \eta, \zeta)$.

To relate operations on D to those on I we need to construct a smooth and invertible mapping, $\Psi : \mathsf{D} \rightarrow \mathsf{I}$, that uniquely relates the two simplices as illustrated in Fig. 1. In the case of a general curvilinear mapping, this can be constructed directly by the use of linear transfinite blending functions. Although lengthy, expressions of these mappings are straightforwardly arrived at by blending parameterized versions of faces, edges, and the vertex-coordinates. For a detailed account of this we refer to [21].

A particularly important and simple case is that of D being straightfaced in which case the mapping becomes

$$\boldsymbol{x} = \Psi(\boldsymbol{\xi}) = -\frac{1+\xi+\eta+\zeta}{2}\boldsymbol{v}_1 + \frac{1+\xi}{2}\boldsymbol{v}_2 + \frac{1+\eta}{2}\boldsymbol{v}_3 + \frac{1+\zeta}{2}\boldsymbol{v}_4 \quad , \tag{11}$$

derived directly by exploiting that any point in the straightfaced tetrahedron can be expressed as a convex sum of the vertices with the weights being the barycentric coordinates (see e.g. [21]).

Once the mapping, $\Psi(\boldsymbol{\xi})$, has been established, we can utilize this to compute the curvilinear metric of the transformation by

$$\frac{\partial \boldsymbol{x}}{\partial \boldsymbol{\xi}}\frac{\partial \boldsymbol{\xi}}{\partial \boldsymbol{x}} = \frac{\partial \Psi(\boldsymbol{\xi})}{\partial \boldsymbol{\xi}}\frac{\partial \boldsymbol{\xi}}{\partial \boldsymbol{x}} = \begin{bmatrix} x_\xi & x_\eta & x_\zeta \\ y_\xi & y_\eta & y_\zeta \\ z_\xi & z_\eta & z_\zeta \end{bmatrix} \begin{bmatrix} \xi_x & \xi_y & \xi_z \\ \eta_x & \eta_y & \zeta_z \\ \zeta_x & \zeta_y & \zeta_z \end{bmatrix} = \begin{bmatrix} 1 & 0 & 0 \\ 0 & 1 & 0 \\ 0 & 0 & 1 \end{bmatrix} \quad .$$

Within this new metric, the divergence of a vector field, $\boldsymbol{F} = (F_x, F_y, F_z)$, is expressed on the well known form

$$\nabla \cdot \boldsymbol{F} = \frac{1}{J}\left[\frac{\partial}{\partial \xi}(J\boldsymbol{F}\cdot\nabla\xi) + \frac{\partial}{\partial \eta}(J\boldsymbol{F}\cdot\nabla\eta) + \frac{\partial}{\partial \zeta}(J\boldsymbol{F}\cdot\nabla\zeta)\right] \quad ,$$

where we have introduced the transformation Jacobian

$$J = \left|\frac{\partial \boldsymbol{x}}{\partial \boldsymbol{\xi}}\right| = \frac{1}{\nabla\xi\cdot(\nabla\eta\times\nabla\zeta)} \quad .$$

The metric also immediately gives outward pointing normal vectors at the 4 faces of D on the form

$$\boldsymbol{n}^a = \nabla\xi + \nabla\eta + \nabla\zeta \quad ,$$

$$\boldsymbol{n}^b = -\nabla\xi \quad , \quad \boldsymbol{n}^c = -\nabla\eta \quad , \quad \boldsymbol{n}^d = -\nabla\zeta \quad .$$

It is worth while paying attention to the special case of the mapping between straightsided tetrahedra, Eq.(11), in which case we realize that

$$\frac{\partial \boldsymbol{x}}{\partial \boldsymbol{\xi}} = \frac{\partial \Psi(\boldsymbol{\xi})}{\partial \boldsymbol{\xi}} = \frac{1}{2}\begin{bmatrix} -\boldsymbol{v}_1^T + \boldsymbol{v}_2^T \\ -\boldsymbol{v}_1^T + \boldsymbol{v}_3^T \\ -\boldsymbol{v}_1^T + \boldsymbol{v}_4^T \end{bmatrix} \quad ,$$

is constant. Thus, the full metric, $\nabla\xi$, $\nabla\eta$, and $\nabla\zeta$, is constant as is the transformation Jacobian, J, i.e., every two straightsided tetrahedra are connected through a simple linear transformation. As we discuss in detail in the appendix, this observation can be exploited to significantly simplify the implementation of the general unstructured scheme by introducing template operators.

Let us finally define a number of different inner products on the curvilinear simplex, D. Consider the two smooth functions, $f[\mathsf{D}] \in \mathsf{C}[\mathsf{D}]$ and $g[\mathsf{D}] \in \mathsf{C}[\mathsf{D}]$ for which $f(\boldsymbol{x}) : \mathsf{D} \rightarrow \mathsf{R}$ and $g(\boldsymbol{x}) : \mathsf{D} \rightarrow \mathsf{R}$. The global inner product, the associated L^2-norm and the inner product over the surface of D are defined as

$$(f,g)_{\mathsf{D}} = \int_{\mathsf{D}} f(\boldsymbol{x})g(\boldsymbol{x})\,d\boldsymbol{x} \quad , \quad (f,f)_{\mathsf{D}} = \|f\|^2_{\mathsf{D}} \quad , \quad (f,g)_{\delta\mathsf{D}} = \oint_{\delta\mathsf{D}} f(\boldsymbol{x})g(\boldsymbol{x})\,d\boldsymbol{x} \quad .$$

These local inner products and norms form the basis for the corresponding global broken measures as

$$(f,g)_{\Omega} = \sum_k (f,g)_{\mathsf{D}^k} \quad , \quad (f,f)_{\Omega} = \sum_k \|f\|^2_{\mathsf{D}^k} = \|f\|^2_{\Omega} \quad ,$$

$$(f,g)_{\delta\Omega} = \sum_k \oint_{\delta\mathsf{D}^k} f(\boldsymbol{x})g(\boldsymbol{x})\,d\boldsymbol{x} \quad ,$$

where K represents the total number of elements used to cover Ω.

3.2. A Multivariate Polynomial Basis on the d-Simplex. With the curvilinear framework in place we can now focus the attention on the development of a high-order/spectral representation of a function defined on the elemental element, I, rather than a general D.

Contrary to the approach taken in [17, 21], where a purely modal approximation is utilized, we shall employ a purely nodal scheme. Hence, we assume that the unknown solutions, $\boldsymbol{q}(\boldsymbol{\xi},t)$, can be well approximated as

$$\boldsymbol{q}_N(\boldsymbol{\xi},t) = \sum_{j=0}^{N} \boldsymbol{q}(\boldsymbol{\xi}_j,t)L_j(\boldsymbol{\xi}) \quad ,$$

where $L_j(\boldsymbol{\xi})$ is the genuine three-dimensional multivariate Lagrange interpolation polynomial, $L_j(\boldsymbol{\xi}) \in \mathsf{P}^3_n$, where

$$\mathsf{P}^3_n = \text{span}\left\{\xi^i\eta^j\zeta^k; i,j,k \geq 0; i+j+k \leq n\right\} \quad ,$$

based on the $N^3_n = N+1$ nodal points, $\boldsymbol{\xi}_j$, given in the interior as well as on the boundary of I. It is straightforward to see that the minimum number of nodal points that will allow this basis to be complete is

$$N^3_n = \frac{1}{6}(n+1)(n+2)(n+3) \quad ,$$

where n signifies the maximum order of the polynomial.

The crucial choice of a nodal set, well suited for Lagrange interpolation within the tetrahedron, is an issue that has received some attention lately with such nodal sets being given in [31] and [29]. The former is derived by using an minimization procedure for the identification of the nodal set that minimizes an approximation to the Lebesque constant while the approach taken in the latter work involves the solution of an electrostatic problem within the tetrahedron. Either procedure results in fully unstructured nodal sets, an example of which is given in Fig. 2, with a large degree of symmetry, exactly N^3_n nodes within the tetrahedron and a very well behaved Lagrange polynomial as measured through the growth of the associated Lebesque constant. Furthermore, both nodal sets include the 4 vertices in I and have exactly $\frac{1}{2}(n+1)(n+2)$ nodes at each of the four faces. This latter property is important as it ensures that a complete two-dimensional polynomial is supported by the nodes on each face.

In this work we have chosen to use the nodal set from [29] as the nodes on which the Lagrange interpolation polynomials are based. These nodal sets are given for n up to 10, corresponding to $N^3_{10} = 286$ nodal points within each tetrahedron and 66 nodal points at each face.

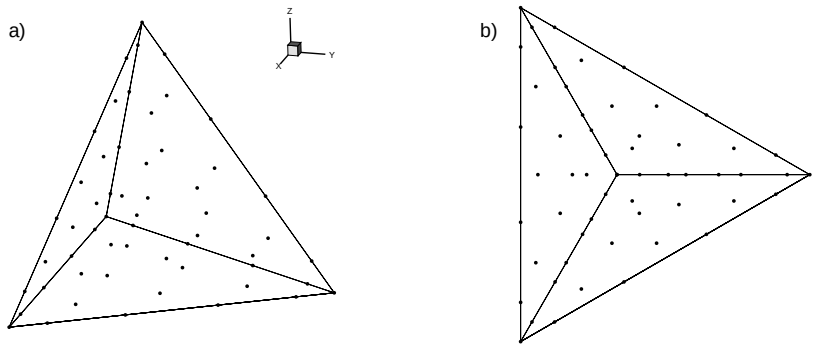

FIG. 2. *Example of nodal set for a 5th order interpolation, i.e., $N_5^3 = 56$ nodes within the tetrahedron. In a) we show a 3D view of the nodes within the tetrahedron while b) gives a top view emphasizing the high degree of symmetry associated with the nodal set.*

Once we have identified a proper nodal set, we can proceed with the formulation of the interpolation which must have the property

$$\mathcal{I}_N^3 f(\boldsymbol{\xi}_j) = f(\boldsymbol{\xi}_j) \quad ,$$

for any $f \in \mathsf{C}[\mathsf{I}]$. For the actual construction of the interpolation polynomials, let us introduce the complete polynomial basis, $p_i(\boldsymbol{\xi}) \in \mathsf{P}_n^3$ and express the interpolation property as

$$\forall i \quad : \quad f(\boldsymbol{\xi}_i) = \sum_{j=0}^{N} \hat{f}_j p_j(\boldsymbol{\xi}_i) \quad , \tag{12}$$

or in compact form

$$\mathrm{V}\hat{\boldsymbol{f}} = \boldsymbol{f} \quad ,$$

where $\hat{\boldsymbol{f}} = [\hat{f}_0, .., \hat{f}_N]^T$ is the vector of expansion coefficients, $\boldsymbol{f} = [f(\boldsymbol{\xi}_0), .., f(\boldsymbol{\xi}_N)]^T$ is the grid vector and $\mathrm{V}_{ij} = p_j(\boldsymbol{\xi}_i)$ is the multi-dimensional generalization of the Vandermonde matrix. Clearly, for the interpolation to exist, V must be nonsingular which is a property that depends solely on the nodal sets. For polynomial interpolation along the line it is well known that $|\mathrm{V}| \neq 0$ provided that the nodes are distinct. Unfortunately, no such simple results are known for polynomial interpolation in I and we shall simply rely on computational verification that the nodal sets indeed allow for the computation of a unique interpolation polynomial[29]. Under this assumption we can likewise express Eq.(12) as

$$\forall i \quad : \quad f(\boldsymbol{\xi}_i) = \sum_{j=0}^{N} f(\boldsymbol{\xi}_i) L_j(\boldsymbol{\xi}_i) \quad , \tag{13}$$

which has to be true for any $f \in \mathsf{C}[\mathsf{I}]$, and in particular $p_i(\boldsymbol{\xi})$ itself. Hence, the Lagrange polynomials can be evaluated at any point, $\boldsymbol{\xi} \in \mathsf{I}$, by solving the dual problem

$$\mathrm{V}^T \boldsymbol{L} = \boldsymbol{p} \quad , \tag{14}$$

where $\boldsymbol{L} = [L_0(\boldsymbol{\xi}), .., L_N(\boldsymbol{\xi})]^T$ and $\boldsymbol{p} = [p_0(\boldsymbol{\xi}), .., p_N(\boldsymbol{\xi})]^T$. This naturally enables the evaluation of $\mathcal{I}_N^3 f(\boldsymbol{\xi})$ anywhere in I by computing $L_j(\boldsymbol{\xi})$ and applying Eq.(13).

In seeking the approximate solution to partial differential equations, the single most important operation is that of computing approximations to spatial derivatives. However, once we have identified a well behaved Lagrange basis, approximations to spatial derivatives evaluated at the grid points, $\boldsymbol{\xi}_i$, is obtained directly through matrix-vector products as

$$\mathcal{I}_n^3 \frac{\partial f}{\partial \xi} \simeq \frac{\partial \mathcal{I}_n^3 f}{\partial \xi} = \mathrm{D}^\xi \boldsymbol{f} \ , \ \mathcal{I}_n^3 \frac{\partial f}{\partial \eta} \simeq \frac{\partial \mathcal{I}_n^3 f}{\partial \eta} = \mathrm{D}^\eta \boldsymbol{f} \ , \ \mathcal{I}_n^3 \frac{\partial f}{\partial \zeta} \simeq \frac{\partial \mathcal{I}_n^3 f}{\partial \zeta} = \mathrm{D}^\zeta \boldsymbol{f} \ ,$$

where the entries of the quadratic differentiation matrices are obtained as

$$\mathrm{D}_{ij}^\xi = \frac{\partial L_j(\boldsymbol{\xi}_i)}{\partial \xi} \ , \ \mathrm{D}_{ij}^\eta = \frac{\partial L_j(\boldsymbol{\xi}_i)}{\partial \eta} \ , \ \mathrm{D}_{ij}^\zeta = \frac{\partial L_j(\boldsymbol{\xi}_i)}{\partial \zeta} \ .$$

The entries can be computed directly by using Eq.(14) and the uniqueness of the polynomials as

$$\mathrm{D}^\xi = \mathrm{P}^\xi \mathrm{V}^{-1} \ , \ \mathrm{D}^\eta = \mathrm{P}^\eta \mathrm{V}^{-1} \ , \ \mathrm{D}^\zeta = \mathrm{P}^\zeta \mathrm{V}^{-1} \ ,$$

where the entries of $\mathrm{P}^{(\xi,\eta,\zeta)}$ are

$$\mathrm{P}_{ij}^\xi = \frac{\partial p_j(\boldsymbol{\xi}_i)}{\partial \xi} \ , \ \mathrm{P}_{ij}^\eta = \frac{\partial p_j(\boldsymbol{\xi}_i)}{\partial \eta} \ , \ \mathrm{P}_{ij}^\zeta = \frac{\partial p_j(\boldsymbol{\xi}_i)}{\partial \zeta} \ . \tag{15}$$

4. A Convergent Scheme for Maxwell's Equations. Having realized high-order formulations of basic operations on the nodal tetrahedron, we are now in a position to develop a scheme suitable for solving linear systems of hyperbolic problems in complex geometries, exemplified by a scheme for solving Maxwell's equations.

To simplify matters, let us express Maxwell's equations, Eq.(3), in conservation form

$$\frac{\partial \boldsymbol{q}}{\partial t} + \nabla \cdot \boldsymbol{F}(\boldsymbol{q}) = \boldsymbol{S} \ , \tag{16}$$

where we have introduced the state vector, $\boldsymbol{q}$, and $\boldsymbol{F}(\boldsymbol{q}) = [F_1(\boldsymbol{q}), F_2(\boldsymbol{q}), F_3(\boldsymbol{q})]^T$, as the flux defined as

$$\boldsymbol{q} = \begin{bmatrix} \varepsilon_r \boldsymbol{E} \\ \mu_r \boldsymbol{H} \end{bmatrix} \ , \ F_i(\boldsymbol{q}) = \begin{bmatrix} -\boldsymbol{e}_i \times \boldsymbol{H} \\ \boldsymbol{e}_i \times \boldsymbol{E} \end{bmatrix} \ ,$$

respectively. Here $\boldsymbol{e}_i$ signifies the three Cartesian unit vectors and $\boldsymbol{S} = [\boldsymbol{S}^E, \boldsymbol{S}^H]^T$ represents body forces, e.g., currents, and terms introduced by the scattered field formulation, Eqs. (7)-(8).

4.1. Central Elements of the Scheme. Let us begin by introducing the nodal basis discussed in the previous section and assume that the statevector, $\boldsymbol{q}$, can be represented as

$$\boldsymbol{q}_N(\boldsymbol{x}, t) = \sum_{j=0}^{N} \boldsymbol{q}(\boldsymbol{x}_j, t) L_j(\boldsymbol{x}) \ ,$$

within each general curvilinear element, D^k.

We shall consider schemes in which we require Eq.(16) to be satisfied in the following way

$$\int_{\mathsf{D}} \left(\frac{\partial \boldsymbol{q}_N}{\partial t} + \nabla \cdot \boldsymbol{F}_N - \boldsymbol{S}_N \right) \phi_i(\boldsymbol{x}) \, d\boldsymbol{x} = \oint_{\delta \mathsf{D}} \psi_i(\boldsymbol{x}) \boldsymbol{G}([\boldsymbol{q}_N]) \, d\boldsymbol{x} \ . \tag{17}$$

Here ϕ_i and ψ_i signify sequences of N functions while $\boldsymbol{G}([\boldsymbol{q}_N])$ is a function of the jump $[\boldsymbol{q}_N]$ of the statevector at the boundary/interface of the element, e.g., if the face is at a solid boundary $[\boldsymbol{q}_N]$ reflects the difference between the prescribed boundary condition and the actual value of the statevector.

Let us emphasizing a few characteristics of this general formulation, Eq.(17). In particular we see that consistency of the scheme is immediate as the right hand side of Eq.(17) vanishes when the exact solution is introduced, i.e., if the inner scheme is consistent so is the full approximation. One should also observe that boundary/interface conditions are not imposed exactly but rather weakly through the penalizing surface integral. Finally we emphasize that in a multi-element context, the formulation is inherently discontinuous, enforcing the interface conditions weakly through the penalizing term and giving rise to a highly parallel formulation of the scheme.

In choosing ϕ_i, ψ_i and $\boldsymbol{G}([\boldsymbol{q}_N])$ one has a tremendous degree of freedom in designing schemes suitable for solving differential equations. In [10] we proposed stable spectral collocation methods with weakly imposed boundary/interface conditions for solving the advection-diffusion equation and the compressible Navier-Stokes equations by choosing $\phi_i(\boldsymbol{x}) = \psi_i(\boldsymbol{x}) = \delta(\boldsymbol{x} - \boldsymbol{x}_i)$ and defining $\boldsymbol{G}([\boldsymbol{q}_N])$ to impose the correct upwind flux conditions. Alternative choices, likewise leading to stable schemes for solving linear conservation laws, were discussed in [28, 29]. There we considered mixed Galerkin-collocation formulations by choosing $\phi_i(\boldsymbol{x}) = L_i(\boldsymbol{x})$, as in a classic Galerkin formulation, but using $\psi_i(\boldsymbol{x}) = \delta(\boldsymbol{x} - \boldsymbol{x}_i)$ to impose the boundary/interface conditions. Upwind flux conditions were used to construct $\boldsymbol{G}([\boldsymbol{q}_N])$.

To formulate a scheme for Maxwell's equations, let us assume that the electric, $\boldsymbol{E}$, and magnetic, $\boldsymbol{H}$, field components can be represented as

$$\boldsymbol{E}_N(\boldsymbol{x},t) = \sum_{j=0}^{N} \boldsymbol{E}(\boldsymbol{x}_j,t) L_j(\boldsymbol{x}) = \sum_{j=0}^{N} \boldsymbol{E}_j(t) L_j(\boldsymbol{x}) \quad ,$$

$$\boldsymbol{H}_N(\boldsymbol{x},t) = \sum_{j=0}^{N} \boldsymbol{H}(\boldsymbol{x}_j,t) L_j(\boldsymbol{x}) = \sum_{j=0}^{N} \boldsymbol{H}_i(t) L_j(\boldsymbol{x}) \quad ,$$

within each general curvilinear element, D^k. Here $\boldsymbol{E}_j(t)$ and $\boldsymbol{H}_j(t)$ represent the time dependent nodal values, i.e., the unknowns of the scheme, while $\boldsymbol{x}_j = \boldsymbol{x}_j(\boldsymbol{\xi}_j)$ are the mapped nodal coordinates.

We shall require that the equations, Eq.(3), be satisfied in the following Galerkin-like way

$$\int_{\mathsf{D}} \left(\frac{\partial \boldsymbol{q}_N}{\partial t} + \nabla \cdot \boldsymbol{F}_N - \boldsymbol{S}_N \right) L_i(\boldsymbol{x})\, d\boldsymbol{x} = \oint_{\delta\mathsf{D}} \tau(\boldsymbol{x}) L_i(\boldsymbol{x}) \hat{\boldsymbol{n}} \cdot [\boldsymbol{F}_N^+]\, d\boldsymbol{x} \quad , \tag{18}$$

where $\boldsymbol{q}_N$, $\boldsymbol{F}_N$, and $\boldsymbol{S}_N$ refers to the approximate state vector, flux and body force, respectively. As in Sec. 3, $L_i(\boldsymbol{x})$ represents the n'th order Lagrange interpolation polynomial, i.e., in the language of the general formulation in Eq.(17) we have $\phi_i(\boldsymbol{x}) = \psi_i(\boldsymbol{x}) = L_i(\boldsymbol{x})$, while we have $\boldsymbol{G}([\boldsymbol{q}_N]) = \tau(\boldsymbol{x}) \hat{\boldsymbol{n}} \cdot [\boldsymbol{F}_N^+]$. Here $\hat{\boldsymbol{n}}$ is the outward pointing normal vector, $\tau(\boldsymbol{x})$ is a free parameter to be specified later, while $[\boldsymbol{F}_N^+]$ reflects the jump in the upwind flux, i.e., we have introduced the splitting, $\boldsymbol{F}_N = \boldsymbol{F}_N^+ + \boldsymbol{F}_N^-$, into the upwind, $\boldsymbol{F}_N^+$, and downwind, $\boldsymbol{F}_N^-$, component of the flux.

It is noteworthy that the classical discontinuous Galerkin formulation [23] is recovered from Eq.(18) by a simple integration by parts and considering all fluxes at interfaces as upwind fluxes, i.e., it is a special case of the much more general approach put forward in Eq.(17).

To understand the exact form of the penalizing flux term, $\hat{\boldsymbol{n}} \cdot [\boldsymbol{F}_N^+]$, it is helpful to recall that

$$\hat{\boldsymbol{n}} \cdot \boldsymbol{F}_N = \begin{bmatrix} -\hat{\boldsymbol{n}} \times \boldsymbol{H}_N \\ \hat{\boldsymbol{n}} \times \boldsymbol{E}_N \end{bmatrix} \ ,$$

i.e., the normal component of the fluxes represents nothing else than the tangential field components and the effect of the right hand side in Eq.(18) is to impose the correct boundary/interface conditions on the tangential field components at the face of the element. It is worth noticing that the unspecified function, $\tau(\boldsymbol{x})$, controls how strongly the conditions are enforced, e.g. if τ is very large the conditions are essentially enforced exactly.

As discussed in Sec. 2 the boundary conditions on the tangential field components, be that in the scattered field or in the total field formulation, require continuity between any two elements regardless of their material properties. This yields the explicit form of the penalizing boundary term as [32]

$$\hat{\boldsymbol{n}} \cdot \left[\boldsymbol{F}_N^+\right] = \begin{cases} \overline{Z}^{-1} \hat{\boldsymbol{n}} \times (Z^+ [\boldsymbol{H}_N] - \hat{\boldsymbol{n}} \times [\boldsymbol{E}_N]) \\ \overline{Y}^{-1} \hat{\boldsymbol{n}} \times (-\hat{\boldsymbol{n}} \times [\boldsymbol{H}_N] - Y^+ [\boldsymbol{E}_N]) \end{cases} \ , \tag{19}$$

where

$$[\boldsymbol{E}_N] = \boldsymbol{E}_N^+ - \boldsymbol{E}_N^- \ , \ [\boldsymbol{H}_N] = \boldsymbol{H}_N^+ - \boldsymbol{H}_N^- \ ,$$

measures the jump in the field values across an interface, i.e., superscript '+' refers to field values from the neighbor element while superscript '-' refers to field values local to the element. To account for the potential differences in material properties in the two elements, we have introduced the local impedance, $Z^{\pm}$, and conductance, $Y^{\pm}$, defined as

$$Z^{\pm} = \frac{1}{Y^{\pm}} = \sqrt{\frac{\mu_r^{\pm}}{\varepsilon_r^{\pm}}} \ ,$$

and the sums

$$\overline{Z} = Z^+ + Z^- \ , \ \overline{Y} = Y^+ + Y^- \ ,$$

of the local impedance and conductance, respectively.

The special case of a perfectly conducting wall is handled in the above formulation be defining a mirror state within the metallic scatterer as

$$\hat{\boldsymbol{n}} \times \boldsymbol{E}_N^+ = -\hat{\boldsymbol{n}} \times \boldsymbol{E}_N^- \ , \ \hat{\boldsymbol{n}} \times \boldsymbol{H}_N^+ = \hat{\boldsymbol{n}} \times \boldsymbol{H}_N^- \ ,$$

to enforce the correct boundary conditions and define the material parameters by $Z^+ = Z^-$.

Now returning to the semi-discrete scheme, Eq.(18), we have an elementwise expression for the electric field

$$\sum_{j=0}^{N} \left(\mathrm{M}_{ij}^{\varepsilon} \frac{d\boldsymbol{E}_j}{dt} - \mathrm{S}_{ij} \times \boldsymbol{H}_j - \mathrm{M}_{ij} \boldsymbol{S}_j^E \right) = \sum_l \mathrm{F}_{il} \left(\hat{\boldsymbol{n}}_l \times \frac{Z_l^+ [\boldsymbol{H}_l] - \hat{\boldsymbol{n}}_l \times [\boldsymbol{E}_l]}{Z_l^+ + Z_l^-} \right) \ , \tag{20}$$

and likewise for the magnetic field components

$$\sum_{j=0}^{N}\left(\mathrm{M}_{ij}^{\mu}\frac{d\boldsymbol{H}_j}{dt}+\mathrm{S}_{ij}\times\boldsymbol{E}_j-\mathrm{M}_{ij}\boldsymbol{S}_j^H\right) = \sum_l \mathrm{F}_{il}\left(\hat{\boldsymbol{n}}_l\times\frac{-\hat{\boldsymbol{n}}_l\times[\boldsymbol{H}_l]-Y_l^+[\boldsymbol{E}_l]}{Y_l^++Y_l^-}\right) \quad . \tag{21}$$

Here we have introduced

$$\mathrm{M}_{ij}^{\varepsilon}=(L_i(\boldsymbol{x}),\varepsilon(\boldsymbol{x})L_j(\boldsymbol{x}))_{\mathsf{D}} \quad , \quad \mathrm{M}_{ij}^{\mu}=(L_i(\boldsymbol{x}),\mu(\boldsymbol{x})L_j(\boldsymbol{x}))_{\mathsf{D}} \quad ,$$

as the material scaled mass-matrices and

$$\mathrm{M}_{ij}=(L_i(\boldsymbol{x}),L_j(\boldsymbol{x}))_{\mathsf{D}} \quad , \quad \mathrm{S}_{ij}=\left(\mathrm{S}_{ij}^x,\mathrm{S}_{ij}^y,\mathrm{S}_{ij}^z\right)=(L_i(\boldsymbol{x}),\nabla L_j(\boldsymbol{x}))_{\mathsf{D}} \quad ,$$

representing the local mass- and stiffness matrix. Note that in the special case where ε_r and μ_r are elementwise constant, we recover $(\mathrm{M}^{\varepsilon},\mathrm{M}^{\mu})=(\varepsilon_r\mathrm{M},\mu_r\mathrm{M})$.

We have, furthermore, introduced the face-based mass matrices

$$\mathrm{F}_{il}=(L_i(\boldsymbol{x}),\tau(\boldsymbol{x})L_l(\boldsymbol{x}))_{\delta\mathsf{D}} \quad ,$$

where the second index is limited to the trace of the nodal set situated at the faces of D.

Expressing Eqs.(20)-(21) in fully explicit form yields

$$\begin{aligned}\frac{d\boldsymbol{E}_N}{dt} =&(\mathrm{M}^{\varepsilon})^{-1}\,\mathrm{S}\times\boldsymbol{H}_N+(\mathrm{M}^{\varepsilon})^{-1}\,\mathrm{M}\boldsymbol{S}^E\\ &+(\mathrm{M}^{\varepsilon})^{-1}\,\mathrm{F}\left(\hat{\boldsymbol{n}}\times\frac{Z^+[\boldsymbol{H}_N]-\hat{\boldsymbol{n}}\times[\boldsymbol{E}_N]}{Z^++Z^-}\right)\Big|_{\delta\mathsf{D}} \quad ,\end{aligned} \tag{22}$$

and

$$\begin{aligned}\frac{d\boldsymbol{H}_N}{dt} =&-(\mathrm{M}^{\mu})^{-1}\,\mathrm{S}\times\boldsymbol{E}_N+(\mathrm{M}^{\mu})^{-1}\,\mathrm{M}\boldsymbol{S}^H\\ &-(\mathrm{M}^{\mu})^{-1}\,\mathrm{F}\left(\hat{\boldsymbol{n}}\times\frac{\hat{\boldsymbol{n}}\times[\boldsymbol{H}_N]+Y^+[\boldsymbol{E}_N]}{Y^++Y^-}\right)\Big|_{\delta\mathsf{D}} \quad .\end{aligned} \tag{23}$$

The discrete operators that need to be initialized are, besides the mass-matrices, M and $\mathrm{M}^{\varepsilon,\mu}$, which can be computed exactly as described in the appendix and inverted straightforwardly. We shall also need

$$(\mathrm{M}^{\varepsilon,\mu})^{-1}\,\mathrm{S}=(\mathrm{M}^{\varepsilon,\mu})^{-1}\,[\mathrm{S}^x,\mathrm{S}^y,\mathrm{S}^z]^T \quad ,$$

representing the general curvilinear differentiation matrix, as well as $(\mathrm{M}^{\varepsilon,\mu})^{-1}\,\mathrm{M}$ for source terms. It is worth noticing that for all straightfaced tetrahedra with constant material parameters, the entries of S can be formed directly by combinations of the classical differentiation matrices introduced in Sec. 3, e.g.,

$$\mathrm{M}^{-1}\mathrm{S}^x=\mathrm{D}^{\xi}\xi_x+\mathrm{D}^{\eta}\eta_x+\mathrm{D}^{\zeta}\zeta_x \quad ,$$

and similarly for $\mathrm{M}^{-1}\mathrm{S}^y$ and $\mathrm{M}^{-1}\mathrm{S}^z$. Hence, as discussed in detail in the appendix, template matrices can be used for the initialization of these operators in all such elements while an individual initialization is required for general curved elements and elements with smoothly varying material parameters.

The same holds true for the face-based operators $\mathrm{M}^{-1}\mathrm{F}$ which again can be precomputed for all straightfaced elements with constant materials by linear scaling from standard template operators for I. The general curvilinear faces requires individual attention.

4.2. Consistency. In analyzing the scheme, Eqs.(22)-(23), it is natural first to consider the global accuracy, and hence consistency, and how it depends on the size of the tetrahedra, i.e., its h-convergence rate, as well as how it scales with the order, n, of the polynomial approximation. To simplify matters we shall assume throughout that all elements involved are straightfaced, i.e., the transformation between D and I is linear. We shall furthermore assume that the material parameters, ε_r and μ_r, be constant on each element, but they can vary freely between elements. We shall later briefly revisit the impact on the results of the analysis of relaxing these assumptions.

Let us introduce the exact solution, $\boldsymbol{q} = [\boldsymbol{E}, \boldsymbol{H}]$, to Maxwell's equations, Eq.(3), as well as its projection, $\mathcal{P}_N \boldsymbol{q} = [\mathcal{P}_N \boldsymbol{E}, \mathcal{P}_N \boldsymbol{H}]^T$, on the space spanned by n-order polynomials, i.e., $\mathcal{P}_N \boldsymbol{q} \in \mathsf{P}_n^3$. Except in very special cases $\mathcal{P}_N \boldsymbol{q}$ will generally be different from the numerical solution, $\boldsymbol{q}_N = [\boldsymbol{E}_N, \boldsymbol{H}_N]^T$, which is the exact solution to the discrete problem, Eqs.(22)-(23).

Before we continue we wish to note that a subtle consequence of using a purely nodal basis, as opposed to a modal basis, is the introduction of a discrete aliasing error in the interpolation of the initial conditions. One could avoid this by reading the nodal values of the Galerkin projection of the initial conditions, computed by using a quadrature of sufficiently high order. However, if the initial conditions are smooth and well resolved this discrete aliasing error is small and we shall not discuss it further in what follows.

As the global error is bounded by the sum of the local, element-wise errors, it suffices to consider the latter. Introducing the exact solution, $\boldsymbol{q} = [\boldsymbol{E}, \boldsymbol{H}]$, to Maxwell's equations, Eq.(3), into the semi-discrete approximation, Eqs.(20)-(21), immediately yields

$$\left(L_i, \boldsymbol{T}^E\right)_{\mathsf{D}} = \left(L_i, \nabla \times \boldsymbol{H} - \mathcal{P}_N \nabla \times \boldsymbol{H}\right)_{\mathsf{D}} + \left(L_i, \boldsymbol{S}^E - \mathcal{P}_N \boldsymbol{S}^E\right)_{\mathsf{D}} \quad ,$$

$$\left(L_i, \boldsymbol{T}^H\right)_{\mathsf{D}} = -\left(L_i, \nabla \times \boldsymbol{E} - \mathcal{P}_N \nabla \times \boldsymbol{E}\right)_{\mathsf{D}} + \left(L_i, \boldsymbol{S}^H - \mathcal{P}_N \boldsymbol{S}^H\right)_{\mathsf{D}} \quad ,$$

where $\boldsymbol{T}^q = \left[\boldsymbol{T}^E, \boldsymbol{T}^H\right]^T$ signifies the truncation error associated with the scheme. Note in particular that the surface terms of Eqs.(20)-(21) vanish identically as the exact solution always has smooth tangential components as dictated by the physics.

To bound the truncation error we shall need the following result [33, 24, 25]

LEMMA 4.1. *Assume that $u \in W^p(\mathsf{D})$, $p \geq 0$. Then there exists a constant, C, dependent on p and the angle condition of D, but independent of u, $h = diam(\mathsf{D})$, and n, such that*

$$\|u - \mathcal{P}_N u\|_{W^q(\mathsf{D})} \leq C \frac{h^{\sigma - q}}{n^{p-q}} \|u\|_{W^p(\mathsf{D})} \quad ,$$

where $\sigma = \min(p, n+1)$ and $0 \leq q \leq \sigma$.

Here we have introduced the standard Sobolev norm

$$\|u\|^2_{W^p(\mathsf{D})} = \sum_{|\alpha| \leq p} \left\| \frac{\partial^{\alpha_1}}{\partial x^{\alpha_1}} \frac{\partial^{\alpha_2}}{\partial x^{\alpha_2}} \frac{\partial^{\alpha_3}}{\partial x^{\alpha_3}} u \right\|^2_{\mathsf{D}} \quad ,$$

with the multi-index, $\alpha = (\alpha_1, \alpha_2, \alpha_3)$.

With this result and the use of the Cauchy-Schwarz inequality we immediately recover the consistency result

THEOREM 4.2. *Assume that the exact solution, $\boldsymbol{q} = [\boldsymbol{E}, \boldsymbol{H}]^T \in W^p(\mathsf{D})$, $p \geq 1$ and that the body forces, $\boldsymbol{S}^q = \left[\boldsymbol{S}^E, \boldsymbol{S}^H\right]^T \in W^p(\mathsf{D})$, $p \geq 0$. Then there exists a constant, C, dependent on p and the angle condition of D, but independent of $\boldsymbol{q}$, $h = diam(\mathsf{D})$, and n, such that*

$$\|\boldsymbol{T}^q\|_{\mathsf{D}} \leq C\left(\frac{h^{\sigma-1}}{n^{p-1}}\|\boldsymbol{q}\|_{W^p(\mathsf{D})} + \frac{h^{\sigma}}{n^{p}}\|\boldsymbol{S}^q\|_{W^p(\mathsf{D})}\right) \quad ,$$

where $\sigma = \min(p, n+1)$.

Hence, if the solution is locally smooth we can expect very rapid convergence in the order of the approximation as well as by decreasing the element size. In particular, if the solution is analytic we can expect to recover full spectral convergence provided the scheme is stable.

4.3. Stability. Let us attend to the issue of semi-discrete stability and define the local energy

$$E^k = \frac{1}{2}\int_{\mathsf{D}^k}\left(\mu|\boldsymbol{H}|^2 + \varepsilon|\boldsymbol{E}|^2\right)\,d\boldsymbol{x} \quad ,$$

and the associated global energy, $E = \sum_k E^k$.

Local elementwise semi-discrete stability is stated as follows

LEMMA 4.3 (Local Stability). *Assume that a solution to Maxwell's equations exists on the domain* D. *If the faces of the element reside away from a perfect conductor, stability of the semi-discrete approximation to Maxwell's equations, Eqs.(22)-(23), is guaranteed provided*

$$\tau \geq \frac{1}{3} \quad .$$

In case one of the faces coincides with a perfect conductor, stability of the semi-discrete approximation is guaranteed if

$$\tau = 1 \quad .$$

Proof. For local stability away from metallic boundaries, it suffices to consider the question of stability for homogeneous boundary conditions, i.e., $\boldsymbol{E}_N^+ = \boldsymbol{H}_N^+ = 0$. Consider Maxwell's equations on the semi-discrete form, Eqs.(20)-(21), multiply from the left with $(\boldsymbol{E}_j, \boldsymbol{H}_j)$ and sum over all the nodes in D to obtain

$$\begin{aligned}\frac{1}{2}\frac{d}{dt}\left(\boldsymbol{E}_N, \varepsilon\boldsymbol{E}_N\right)_{\mathsf{D}} &= \left(\boldsymbol{E}_N, \nabla\times\boldsymbol{H}_N\right)_{\mathsf{D}} + \left(\boldsymbol{E}_N, \boldsymbol{S}^E\right)_{\mathsf{D}} \\ &\quad - \oint_{\delta\mathsf{D}} \tau\boldsymbol{E}_N\cdot\left(\hat{\boldsymbol{n}}\times\frac{Z^+\boldsymbol{H}_N - \hat{\boldsymbol{n}}\times\boldsymbol{E}_N}{Z^+ + Z^-}\right)\,d\boldsymbol{x} \quad ,\end{aligned}$$

and

$$\begin{aligned}\frac{1}{2}\frac{d}{dt}\left(\boldsymbol{H}_N, \mu\boldsymbol{H}_N\right)_{\mathsf{D}} &= -\left(\boldsymbol{H}_N, \nabla\times\boldsymbol{E}_N\right)_{\mathsf{D}} + \left(\boldsymbol{H}_N, \boldsymbol{S}^H\right)_{\mathsf{D}} \\ &\quad + \oint_{\delta\mathsf{D}} \tau\boldsymbol{H}_N\cdot\left(\hat{\boldsymbol{n}}\times\frac{Y^+\boldsymbol{E}_N + \hat{\boldsymbol{n}}\times\boldsymbol{H}_N}{Y^+ + Y^-}\right)\,d\boldsymbol{x} \quad .\end{aligned}$$

Adding the two contributions and applying the the divergence theorem yields

$$\begin{aligned}\frac{d}{dt}E^k =& \oint_{\delta\mathsf{D}}(1-\tau)\hat{\boldsymbol{n}}\cdot\left(\boldsymbol{H}_N\times\boldsymbol{E}_N\right)\,d\boldsymbol{x} \\ &+ \oint_{\delta\mathsf{D}}\left(\frac{\tau}{Z}\boldsymbol{E}_N\cdot\hat{\boldsymbol{n}}\times\hat{\boldsymbol{n}}\times\boldsymbol{E}_N + \frac{\tau}{Y}\boldsymbol{H}_N\cdot\hat{\boldsymbol{n}}\times\hat{\boldsymbol{n}}\times\boldsymbol{H}_N\right)\,d\boldsymbol{x} \\ &+ \left(\boldsymbol{E}_N, \boldsymbol{S}^E\right)_{\mathsf{D}} + \left(\boldsymbol{H}_N, \boldsymbol{S}^H\right)_{\mathsf{D}} \quad .\end{aligned}$$

Using standard vector identities this simplifies as

$$\frac{d}{dt}E^k = -\oint_{\delta\mathsf{D}} \left((1-\tau)\boldsymbol{H}_N \cdot \hat{\boldsymbol{n}} \times \boldsymbol{E}_N + \frac{\tau}{\overline{\overline{Z}}}|\hat{\boldsymbol{n}} \times \boldsymbol{E}_N|^2 + \frac{\tau}{\overline{\overline{Y}}}|\hat{\boldsymbol{n}} \times \boldsymbol{H}_N|^2 \right) d\boldsymbol{x} + \left(\boldsymbol{E}_N, \boldsymbol{S}^E\right)_{\mathsf{D}} + \left(\boldsymbol{H}_N, \boldsymbol{S}^H\right)_{\mathsf{D}} \ .$$

To ensure semi-discrete stability it suffices to require that

$$(1-\tau)\boldsymbol{H}_N^T \mathrm{R} \boldsymbol{E}_N + \frac{\tau}{\overline{\overline{Z}}}\boldsymbol{E}_N^T \mathrm{R}^T \mathrm{R} \boldsymbol{E}_N + \frac{\tau}{\overline{\overline{Y}}}\boldsymbol{H}_N^T \mathrm{R}^T \mathrm{R} \boldsymbol{H}_N \geq 0 \ , \tag{24}$$

where we have introduced the rotation matrix

$$\mathrm{R} = \mathrm{R}(\hat{\boldsymbol{n}}) = \begin{bmatrix} 0 & -n_z & n_y \\ n_z & 0 & -n_x \\ -n_y & n_x & 0 \end{bmatrix} \ .$$

Expressing the quadratic form, Eq.(24), as $\boldsymbol{q}_N^T \mathrm{A} \boldsymbol{q}_N$ with A reflecting Eq.(24), one recovers the first two eigenvalues of A as $\lambda_{1,2}(\mathrm{A}) = 0$ while the remaining are given as

$$\lambda_{3,4} = \frac{\tau(1+\overline{Z}) \pm \sqrt{\tau^2(1+\overline{Z})^2 + \overline{Z}^2\left(-3\tau^2 - 2\tau + 1\right)}}{2\overline{Z}} \ ,$$

and

$$\lambda_{5,6} = \frac{\tau(1+\overline{Y}) \pm \sqrt{\tau^2(1+\overline{Y})^2 + \overline{Y}^2\left(-3\tau^2 - 2\tau + 1\right)}}{2\overline{Y}} \ .$$

Hence, a sufficient condition for stability clearly is that $\tau \geq 0$ and $-3\tau^2 - 2\tau + 1 \leq 0$, i.e.,

$$\tau \geq \frac{1}{3} \ .$$

In case a face resides at a metallic conductor we employ the boundary conditions

$$\hat{\boldsymbol{n}} \times \boldsymbol{E}_N^- = -\hat{\boldsymbol{n}} \times \boldsymbol{E}_N^+ \ , \ \ \hat{\boldsymbol{n}} \times \boldsymbol{H}_N^- = \hat{\boldsymbol{n}} \times \boldsymbol{H}_N^+ \ ,$$

and $Z^+ = Z^- = Z$, $Y^+ = Y^- = Y$.

Following the exact same procedure as above, we recover the constraint

$$(1-\tau)\boldsymbol{H}_N^T \mathrm{R} \boldsymbol{E} + \frac{\tau}{2Z}\boldsymbol{E}_N^T \boldsymbol{R}^T \boldsymbol{R} \boldsymbol{E}_N \geq 0 \ .$$

Computing the eigenvalues of the corresponding quadratic form yields two pairs of the form

$$\lambda_1 = 0 \ , \ \ \lambda_{2,3} = \frac{\tau}{Z} \pm \frac{1}{Z}\sqrt{\tau^2 + Z^2(\tau-1)^2} \ .$$

Clearly, the only way to guarantee positivity of the eigenvalues and hence the quadratic form is to choose $\tau = 1$. □

The result on local, elementwise stability, only supplies a necessary but not sufficient condition for stability. To understand the issue of global stability we must also consider the influence of the coupling between the individual elements.

LEMMA 4.4 (Face Stability). *Assume that a solution to the Maxwell's equations exists on a domain consisting of two elements sharing one common face. Stability of the semi-discrete approximation of Maxwell's equations, Eqs.(22)-(23), on this domain is guaranteed provided*

$$\tau = 1 \ .$$

Proof. Consider Maxwell's equations on the semi-discrete form, Eqs.(20)-(21). Multiply from the left with $(\boldsymbol{E}_j, \boldsymbol{H}_j)$ and sum over all the nodes in D to obtain

$$\begin{aligned}\frac{1}{2}\frac{d}{dt}\left(\boldsymbol{E}_N^-, \varepsilon \boldsymbol{E}_N^-\right)_{\mathsf{D}} &= \left(\boldsymbol{E}_N^-, \nabla \times \boldsymbol{H}_N^-\right)_{\mathsf{D}} + \left(\boldsymbol{E}_N^-, \boldsymbol{S}^E\right)_{\mathsf{D}} \\ &\quad + \oint_{\delta\mathsf{D}} \tau \boldsymbol{E}_N^- \cdot \left(\hat{\boldsymbol{n}}^- \times \frac{Z^+[\boldsymbol{H}_N] - \hat{\boldsymbol{n}}^- \times [\boldsymbol{E}_N]}{Z^+ + Z^-}\right) d\boldsymbol{x} \ ,\end{aligned}$$

and

$$\begin{aligned}\frac{1}{2}\frac{d}{dt}\left(\boldsymbol{H}_N^-, \mu \boldsymbol{H}_N^-\right)_{\mathsf{D}} &= -\left(\boldsymbol{H}_N^-, \nabla \times \boldsymbol{E}_N^-\right)_{\mathsf{D}} + \left(\boldsymbol{H}_N^-, \boldsymbol{S}^H\right)_{\mathsf{D}} \\ &\quad - \oint_{\delta\mathsf{D}} \tau \boldsymbol{H}_N^- \cdot \left(\hat{\boldsymbol{n}}^- \times \frac{Y^+[\boldsymbol{E}_N] + \hat{\boldsymbol{n}} \times [\boldsymbol{H}_N]}{Y^+ + Y^-}\right) d\boldsymbol{x} \ .\end{aligned}$$

Addition of the two contributions, application of the divergence theorem and standard vector identities yields

$$\begin{aligned}\frac{d}{dt}E^k =& \oint_{\delta\mathsf{D}} (1-\tau)\hat{\boldsymbol{n}}^- \cdot \left(\boldsymbol{H}_N^- \times \boldsymbol{E}_N^-\right) \\ &+\tau\left(\frac{Y^+}{\overline{Y}}\boldsymbol{E}_N^- \cdot \left(\hat{\boldsymbol{n}}^- \times \boldsymbol{H}_N^+\right) - \frac{Z^+}{\overline{Z}}\boldsymbol{H}_N^- \cdot \left(\hat{\boldsymbol{n}}^- \times \boldsymbol{E}_N^+\right)\right) \\ &-\tau\left(\frac{1}{\overline{Z}}\boldsymbol{E}_N^- \cdot \left(\hat{\boldsymbol{n}}^- \times \left(\hat{\boldsymbol{n}}^- \times [\boldsymbol{E}_N]\right)\right) + \frac{1}{\overline{Y}}\boldsymbol{H}_N^- \cdot \left(\hat{\boldsymbol{n}}^- \times \left(\hat{\boldsymbol{n}}^- \times [\boldsymbol{H}_N]\right)\right)\right) d\boldsymbol{x} \\ &+\left(\boldsymbol{E}_N^-, \boldsymbol{S}^E\right)_{\mathsf{D}} + \left(\boldsymbol{H}_N^-, \boldsymbol{S}^H\right)_{\mathsf{D}} \ .\end{aligned}$$

To understand the stability of a common edge, it suffices to consider the case where $\boldsymbol{S}^E = \boldsymbol{S}^H = 0$. Adding the contribution from two edges, utilizing that $\hat{\boldsymbol{n}}^- = -\hat{\boldsymbol{n}}^+$, yields

$$\begin{aligned}\frac{d}{dt}E =& \oint_{\delta\mathsf{D}} (1-\tau)\left(\hat{\boldsymbol{n}}^- \cdot \boldsymbol{H}_N^- \times \boldsymbol{E}_N^- - \hat{\boldsymbol{n}}^- \cdot \boldsymbol{H}_N^+ \times \boldsymbol{E}_N^+\right) \\ &+\frac{\tau}{\overline{Z}}[\boldsymbol{E}_N] \cdot \hat{\boldsymbol{n}}^- \times \hat{\boldsymbol{n}}^- \times [\boldsymbol{E}_N] + \frac{\tau}{\overline{Y}}[\boldsymbol{H}_N] \cdot \hat{\boldsymbol{n}}^- \times \hat{\boldsymbol{n}}^- \times [\boldsymbol{H}_N]\, d\boldsymbol{x} \\ =& -\oint_{\delta\mathsf{D}} (1-\tau)\hat{\boldsymbol{n}}^- \cdot \left(\boldsymbol{H}_N^+ \times \boldsymbol{E}_N^+ - \boldsymbol{H}_N^- \times \boldsymbol{E}_N^-\right) \\ &-\frac{\tau}{\overline{Z}}|\hat{\boldsymbol{n}}^- \times [\boldsymbol{E}_N]|^2 - \frac{\tau}{\overline{Y}}|\hat{\boldsymbol{n}}^- \times [\boldsymbol{H}_N]|^2\, d\boldsymbol{x} \ .\end{aligned}$$

A sufficient condition for this to be negative is

$$\begin{aligned}&(1-\tau)\left(\left(\boldsymbol{H}_N^-\right)^T \mathrm{R}\boldsymbol{E}_N^- - \left(\boldsymbol{H}_N^+\right)^T \mathrm{R}\boldsymbol{E}_N^+\right) + \\ &\qquad \frac{\tau}{\overline{Z}}[\boldsymbol{E}_N]^T \mathrm{R}^T \mathrm{R}[\boldsymbol{E}_N]^T + \frac{\tau}{\overline{Y}}[\boldsymbol{H}_N]^T \mathrm{R}^T \mathrm{R}[\boldsymbol{H}_N]^T \geq 0 \ .\end{aligned}$$

Inspection reveals that by defining $\boldsymbol{q} = [\boldsymbol{E}_N^+, \boldsymbol{E}_N^-, \boldsymbol{H}_N^+, \boldsymbol{H}_N^-]^T$, the condition may be expressed is given as a symmetric quadratic form, i.e., it suffices to choose τ such that all eigenvalues of A are non-negative. Leaving out the lengthy and purely algebraic manipulations, we consider the resulting two sets of eigenvalues of A given as

$$\lambda_{1,2} = 0 \ , \ \lambda_{3,4} = \frac{\tau}{\overline{Z}} \pm \frac{1}{2\overline{Z}} \sqrt{4\tau^2 + \overline{Z}(\tau - 1)^2} \ ,$$

and

$$\lambda_{5,6} = \frac{\tau}{\overline{Y}} \pm \frac{1}{2\overline{Y}} \sqrt{4\tau^2 + \overline{Y}(\tau - 1)^2} \ .$$

Clearly, the choice of $\tau = 1$ is the only feasible solution that ensures stability of the upwind scheme used for connecting the elements. □

With these results in place, we can now state

THEOREM 4.5 (Global Stability). *Assume that a unique solution to Maxwell's equations exists in the general domain, Ω. Assume furthermore that the boundary of Ω is either periodic or terminated with a perfectly conducting boundary.*

Then the semi-discrete approximation to Maxwell's equations, Eqs.(22)-(23), is globally stable in the sense that

$$\frac{d}{dt} E \leq C \left(E + \left\| \boldsymbol{S}^E \right\|_\Omega^2 + \left\| \boldsymbol{S}^H \right\|_\Omega^2 \right) \ ,$$

provided only that

$$\tau = 1 \ .$$

Proof. As each face is counted only once, the result follows directly by summation over the all the faces and the application of Lemma 4.3 and Lemma 4.4

$$\begin{aligned} \frac{d}{dt} E &\leq \sum_k \left(\boldsymbol{E}_N, \boldsymbol{S}^E \right)_{\mathsf{D}^k} + \left(\boldsymbol{H}_N, \boldsymbol{S}^H \right)_{\mathsf{D}^k} \\ &\leq C \left(E + \left\| \boldsymbol{S}^E \right\|_\Omega^2 + \left\| \boldsymbol{S}^H \right\|_\Omega^2 \right) \ , \end{aligned}$$

using that $\left(\boldsymbol{E}_N, \boldsymbol{S}^E \right)_\mathsf{D} \leq C(\|\boldsymbol{E}_N\|_\mathsf{D}^2 + \left\| \boldsymbol{S}^E \right\|_\mathsf{D}^2)$, $\|\boldsymbol{E}_N\|_\mathsf{D}^2 \leq C \left(\boldsymbol{E}_N, \varepsilon_r \boldsymbol{E}_N \right)_\mathsf{D}$ since $\varepsilon \geq 1$. A similar line of reasoning is applicable for $\left(\boldsymbol{H}_N, \boldsymbol{S}^H \right)_\mathsf{D}$ and the result on global stability follows. □

4.4. Convergence. Having established consistency as well as stability in equivalent norms, convergence follows directly from the equivalence theorem with a bound on the local error

$$\varepsilon_\mathsf{D}(t) = \|\boldsymbol{E}(t) - \boldsymbol{E}_N(t)\|_\mathsf{D} + \|\boldsymbol{H}(t) - \boldsymbol{H}_N(t)\|_\mathsf{D} \ ,$$

of the form

$$\varepsilon_\mathsf{D}(t) \leq C e^{\alpha t} \left(\varepsilon_\mathsf{D}(0) + \int_0^t \|\boldsymbol{T}^q(s)\|_\mathsf{D} \, ds \right) \ ,$$

and global convergence is hence established up to exponential growth in time as is typical for Lax-type stability results.

As it turns out, however, we can do better and recover a sharp bound for the growth in time by generalizing ideas first put forward in the context of finite difference methods [34]. To realize this, let us make the natural split of the elementwise error as

$$\begin{aligned}\varepsilon_{\mathsf{D}} &\leq (\|\boldsymbol{E}-\mathcal{P}_N\boldsymbol{E}\|_{\mathsf{D}}+\|\boldsymbol{H}-\mathcal{P}_N\boldsymbol{H}\|_{\mathsf{D}})+(\|\mathcal{P}_N\boldsymbol{E}-\boldsymbol{E}_N\|_{\mathsf{D}}+\|\mathcal{P}_N\boldsymbol{N}-\boldsymbol{H}_N\|_{\mathsf{D}})\\ &= \varepsilon^a_{\mathsf{D}}+\varepsilon^b_{\mathsf{D}}\quad,\end{aligned}$$

where $\varepsilon^a_{\mathsf{D}}$ is due to the error introduced by the polynomial approximation of the exact solution while $\varepsilon^b_{\mathsf{D}}$ measures the errors associated with the semi-discrete approximation of Maxwell's equations.

To bound $\varepsilon^a_{\mathsf{D}}$ we need only recall Lemma 4.1 to state

LEMMA 4.6. *Assume that* $\boldsymbol{q}=[\boldsymbol{E},\boldsymbol{H}]^T\in W^p(\mathsf{D})$. *Then there exists a constant,* C, *dependent on* p *and the angle condition of* D, *but independent of* $\boldsymbol{q}$, $h=diam(\mathsf{D})$, *and* n, *such that*

$$\|\boldsymbol{q}-\mathcal{P}_N\boldsymbol{q}\|_{\mathsf{D}}\leq C\frac{h^\sigma}{n^p}\|\boldsymbol{q}\|_{W^p(\mathsf{D})}\quad,$$

where $\sigma=\min(p,n+1)$ *and* $p\geq 0$.

To arrive at a bound for $\varepsilon^b_{\mathsf{D}}$, let us first consider the projection of the truncation error, $\mathcal{P}_N\boldsymbol{T}^q=\left[\mathcal{P}_N\boldsymbol{T}^E,\mathcal{P}_N\boldsymbol{T}^H\right]^T$, on the form

$$\begin{aligned}\left(L_i,\mathcal{P}_N\boldsymbol{T}^E\right)_{\mathsf{D}} =&(L_i,\mathcal{P}_N\nabla\times\boldsymbol{H}-\mathcal{P}_N\nabla\times\mathcal{P}_N\boldsymbol{H})_{\mathsf{D}}\\ &-\frac{1}{\overline{\overline{Z}}}\left(L_i,\hat{\boldsymbol{n}}\times\left(Z^+[\mathcal{P}_N\boldsymbol{H}]-\hat{\boldsymbol{n}}\times[\mathcal{P}_N\boldsymbol{E}]\right)\right)_{\delta\mathsf{D}}\quad,\end{aligned}\tag{25}$$

$$\begin{aligned}\left(L_i,\mathcal{P}_N\boldsymbol{T}^H\right)_{\mathsf{D}} =&-(L_i,\mathcal{P}_N\nabla\times\boldsymbol{E}-\mathcal{P}_N\nabla\times\mathcal{P}_N\boldsymbol{E})_{\mathsf{D}}\\ &-\frac{1}{\overline{\overline{Y}}}\left(L_i,\hat{\boldsymbol{n}}\times\left(-Y^+[\mathcal{P}_N\boldsymbol{E}]-\hat{\boldsymbol{n}}\times[\mathcal{P}_N\boldsymbol{H}]\right)\right)_{\delta\mathsf{D}}\quad.\end{aligned}\tag{26}$$

This is derived by introducing $\mathcal{P}_N\boldsymbol{q}$ into the semi-discrete scheme, Eqs.(20)-(21), exploiting that $\boldsymbol{q}$ satisfies Maxwell's equations, Eq.(3).

The projection of the truncation error can be bounded by the exact solution as

LEMMA 4.7. *Assume that* $\boldsymbol{q}=[\boldsymbol{E},\boldsymbol{H}]^T\in W^p(\mathsf{D}), p\geq 3/2$. *Then there exists a constant,* C, *dependent on* p, *the angle condition of* D *and the local material properties,* ε_r,μ_r, *but independent of* $\boldsymbol{q}$, $h=diam(\mathsf{D})$, *and* n, *such that*

$$\|\mathcal{P}_N\boldsymbol{T}^q\|_{\mathsf{D}}\leq C\frac{h^{\sigma-1}}{n^{p-3/2}}\|\boldsymbol{q}\|_{W^p(\mathsf{D})}\quad,$$

where $\sigma=\min(p,n+1)$.

Proof. We need only establish the result for $\mathcal{P}_N\boldsymbol{T}^E$, Eq.(25), as the derivation of the result for $\mathcal{P}_N\boldsymbol{T}^E$ following identical lines.

As $\mathcal{P}_N\boldsymbol{T}^E\in\mathsf{P}^3_n=\sum_j\boldsymbol{T}^E_jL_j(\boldsymbol{x})$ we can multiply from the left with $\boldsymbol{T}^E_j$ and sum over all the nodes to recover

$$\left\|\mathcal{P}_N \boldsymbol{T}^E\right\|_{\mathsf{D}}^2 = \left(\mathcal{P}_N \boldsymbol{T}^E, \mathcal{P}_N \nabla \times (\boldsymbol{H} - \mathcal{P}_N \boldsymbol{H})\right)_{\mathsf{D}} - \frac{1}{\overline{\overline{Z}}} \left(\mathcal{P}_N \boldsymbol{T}^E, \hat{\boldsymbol{n}} \times \left(Z^+[\mathcal{P}_N \boldsymbol{H}] - \hat{\boldsymbol{n}} \times [\mathcal{P}_N \boldsymbol{E}]\right)\right)_{\delta\mathsf{D}} \quad .$$

Using the Cauchy-Schwarz inequality and the estimate [25]

$$\|\boldsymbol{q}_N\|_{\delta\mathsf{D}} \leq C \frac{n}{h^{1/2}} \|\boldsymbol{q}_N\|_{\mathsf{D}} \quad ,$$

for all $\boldsymbol{q} \in \mathsf{P}_n^3(\mathsf{D})$, $h = \mathrm{diam}(\mathsf{D})$, we recover

$$\left\|\mathcal{P}_N \boldsymbol{T}^E\right\|_{\mathsf{D}} \leq C_1 \|\mathcal{P}_N \nabla \times (\boldsymbol{H} - \mathcal{P}_N \boldsymbol{H})\|_{\mathsf{D}} + C_2 \frac{n}{h^{1/2}} \frac{1}{\overline{\overline{Z}}} \left\|Z^+[\mathcal{P}_N \boldsymbol{H}_\tau] - [\mathcal{P}_N \boldsymbol{E}_\tau]\right\|_{\delta\mathsf{D}} \quad , \tag{27}$$

where we for simplicity have introduced the tangential components

$$\boldsymbol{E}_\tau = \hat{\boldsymbol{n}} \times \boldsymbol{E} \quad , \quad \boldsymbol{H}_\tau = \hat{\boldsymbol{n}} \times \boldsymbol{H} \quad .$$

To bound the first term we invoke Lemma 4.1 to obtain

$$\|\mathcal{P}_N \nabla \times (\boldsymbol{H} - \mathcal{P}_N \boldsymbol{H})\|_{\mathsf{D}} \leq \|\nabla \times (\boldsymbol{H} - \mathcal{P}_N \boldsymbol{H})\|_{\mathsf{D}} \leq C \frac{h^{\sigma-1}}{n^{p-1}} \|\boldsymbol{H}\|_{W^p(\mathsf{D})} \, . \tag{28}$$

Consider now terms of the type

$$\|[\mathcal{P}_N \boldsymbol{E}_\tau]\|_{\delta\mathsf{D}} \leq \left\|\mathcal{P}_N \boldsymbol{E}_\tau^+ - \boldsymbol{E}_\tau^+\right\|_{\delta\mathsf{D}} + \left\|\mathcal{P}_N \boldsymbol{E}_\tau^- - \boldsymbol{E}_\tau^-\right\|_{\delta\mathsf{D}} \quad ,$$

where $\boldsymbol{E}_\tau^+ = \boldsymbol{E}_\tau^- = \boldsymbol{E}_\tau$ represents the exact solution at $\delta\mathsf{D}$. Recalling the trace inequality [35]

$$\|q\|_{\delta\mathsf{D}}^2 \leq C \left(\|q\|_{\mathsf{D}} \|\nabla q\|_{\mathsf{D}} + h^{-1} \|q\|_{\mathsf{D}}^2\right) \quad , \quad q \in W^1(\mathsf{D}) \quad ,$$

implies that

$$\|q - \mathcal{P}_N q\|_{\delta\mathsf{D}}^2 \leq C \left(\|q - \mathcal{P}_N q\|_{\mathsf{D}} \|q - \mathcal{P}_N q\|_{W^1(\mathsf{D})} + h^{-1} \|q - \mathcal{P}_N q\|_{\mathsf{D}}^2\right) \quad ,$$

and we recover by combination with Lemma 4.1 the bound

$$\|[\mathcal{P}_N \boldsymbol{E}_\tau]\|_{\delta\mathsf{D}} \leq C \frac{h^{\sigma-1/2}}{n^{p-1/2}} \|\boldsymbol{E}\|_{W^p(\mathsf{D})} \quad .$$

Combining this with Eqs.(27)-(28) one obtains the result

$$\left\|\mathcal{P}_N \boldsymbol{T}^E\right\|_{\mathsf{D}} \leq C_1 \frac{h^{\sigma-1}}{n^{p-1}} \|\boldsymbol{H}\|_{W^p(\mathsf{D})} + C_2 \frac{h^{\sigma-1}}{n^{p-3/2}} \left(\|\boldsymbol{E}\|_{W^p(\mathsf{D})} + \|\boldsymbol{H}\|_{W^p(\mathsf{D})}\right) \quad ,$$

where (C_1, C_2) are independent of h and n but C_2 depends on the local material properties $(Z^\pm, Y^\pm)$.

The result for $\left\|\mathcal{P}_N \boldsymbol{T}^H\right\|_{\mathsf{D}}$ is recovered in the same way, yielding the result

$$\left\|\mathcal{P}_N \boldsymbol{T}^H\right\|_{\mathsf{D}} \leq C_1 \frac{h^{\sigma-1}}{n^{p-1}} \|\boldsymbol{E}\|_{W^p(\mathsf{D})} + C_2 \frac{h^{\sigma-1}}{n^{p-3/2}} \left(\|\boldsymbol{E}\|_{W^p(\mathsf{D})} + \|\boldsymbol{H}\|_{W^p(\mathsf{D})}\right) \quad ,$$

hence establishing the stated result. □

Let us now return to the original quest for an improved convergence estimate and consider the error equation

$$
\begin{aligned}
(29) \qquad \left(L_i, \varepsilon \frac{\partial}{\partial t}\left(\mathcal{P}_N \boldsymbol{E} - \boldsymbol{E}_N\right)\right)_{\mathsf{D}} =& \left(L_i, \mathcal{P}_N \nabla \times \left(\mathcal{P}_N \boldsymbol{E} - \boldsymbol{E}_N\right)\right)_{\mathsf{D}} \\
&+ \frac{1}{\overline{\overline{Z}}}\left(L_i, \hat{\boldsymbol{n}} \times \left(Z^+[\mathcal{P}_N \boldsymbol{H} - \boldsymbol{H}_N] - \hat{\boldsymbol{n}} \times [\mathcal{P}_N \boldsymbol{E} - \boldsymbol{E}_N]\right)\right)_{\delta \mathsf{D}} \\
&+ \left(L_i, \mathcal{P}_N \boldsymbol{T}^E\right)_{\mathsf{D}} \quad ,
\end{aligned}
$$

for the electric field and similarly for the magnetic field

$$
\begin{aligned}
(30) \qquad \left(L_i, \mu \frac{\partial}{\partial t}\left(\mathcal{P}_N \boldsymbol{H} - \boldsymbol{H}_N\right)\right)_{\mathsf{D}} =& -\left(L_i, \mathcal{P}_N \nabla \times \left(\mathcal{P}_N \boldsymbol{H} - \boldsymbol{H}_N\right)\right)_{\mathsf{D}} \\
&- \frac{1}{\overline{\overline{Y}}}\left(L_i, \hat{\boldsymbol{n}} \times \left(Y^+[\mathcal{P}_N \boldsymbol{E} - \boldsymbol{E}_N] + \hat{\boldsymbol{n}} \times [\mathcal{P}_N \boldsymbol{H} - \boldsymbol{H}_N]\right)\right)_{\delta \mathsf{D}} \\
&+ \left(L_i, \mathcal{P}_N \boldsymbol{T}^H\right)_{\mathsf{D}} \quad .
\end{aligned}
$$

The combination of these expressions with Lemma 4.7 and the methodology of the stability proof in Sec. 4.3 yields the improved convergence result

THEOREM 4.8. *Assume that a solution, $\boldsymbol{q} \in W^p(\mathsf{D})$, $p \geq 3/2$ to Maxwell's equations in $\Omega = \bigcup_k \mathsf{D}^k$ exists. Then the numerical solution, $\boldsymbol{q}_N$, to the semi-discrete approximation Eqs.(22)-(23) converges to the exact solution and the global error, $\sum_k \|\boldsymbol{q} - \boldsymbol{q}_N\|_{\mathsf{D}^k}$ is bounded as*

$$
\begin{aligned}
\sum_k \|\boldsymbol{q}(t) - \boldsymbol{q}_N(t)\|_{\mathsf{D}^k} \leq & C \sum_k \Big(\|\boldsymbol{q}(t) - \mathcal{P}_N \boldsymbol{q}(t)\|_{\mathsf{D}^k} \\
&+ \|\mathcal{P}_N \boldsymbol{q}(0) - \boldsymbol{q}_N(0)\|_{\mathsf{D}^k} + t \max_{s \in [0,t]} \|\boldsymbol{T}^q(s)\|_{\mathsf{D}^k} \Big) \\
\leq & C \sum_k \left(\frac{h^\sigma}{n^p} \|\boldsymbol{q}(0)\|_{W^p(\mathsf{D}^k)} + t \frac{h^{\sigma-1}}{n^{p-3/2}} \max_{s \in [0,t]} \|\boldsymbol{q}(s)\|_{W^p(\mathsf{D}^k)} \right) \quad ,
\end{aligned}
$$

where C depends on the material properties and the angle conditions of the elements but not on h and n.

Proof. Since $\mathcal{P}_N \boldsymbol{E} - \boldsymbol{E}_N \in \mathsf{P}_n^3$ and $\mathcal{P}_N \boldsymbol{H} - \boldsymbol{H}_N \in \mathsf{P}_n^3$ we can use these as elementwise test functions in Eq.(29) and Eq.(30), respectively, to obtain

$$
\begin{aligned}
&\frac{1}{2}\frac{d}{dt}\left(\left(\mathcal{P}_N \boldsymbol{E} - \boldsymbol{E}_N, \varepsilon\left(\mathcal{P}_N \boldsymbol{E} - \boldsymbol{E}_N\right)\right)_{\mathsf{D}} + \left(\mathcal{P}_N \boldsymbol{H} - \boldsymbol{H}_N, \varepsilon\left(\mathcal{P}_N \boldsymbol{H} - \boldsymbol{H}_N\right)\right)_{\mathsf{D}}\right) \\
&= \oint_{\delta \mathsf{D}} \Big(\left(\hat{\boldsymbol{n}} \cdot \left(\mathcal{P}_N \boldsymbol{H} - \boldsymbol{H}_N\right)\right) \times \left(\mathcal{P}_N \boldsymbol{E} - \boldsymbol{E}_N\right) \\
&\quad + \frac{1}{\overline{\overline{Z}}}\left(\mathcal{P}_N \boldsymbol{E} - \boldsymbol{E}_N\right) \cdot \hat{\boldsymbol{n}} \times \left(Z^+[\mathcal{P}_N \boldsymbol{H} - \boldsymbol{H}_N] - \hat{\boldsymbol{n}} \times [\mathcal{P}_N \boldsymbol{E} - \boldsymbol{E}_N]\right) \\
&\quad - \frac{1}{\overline{\overline{Y}}}\left(\mathcal{P}_N \boldsymbol{H} - \boldsymbol{H}_N\right) \cdot \hat{\boldsymbol{n}} \times \left(Y^+[\mathcal{P}_N \boldsymbol{E} - \boldsymbol{E}_N] + \hat{\boldsymbol{n}} \times [\mathcal{P}_N \boldsymbol{H} - \boldsymbol{H}_N]\right) \Big) \, d\boldsymbol{x} \\
&\quad \left(\mathcal{P}_N \boldsymbol{E} - \boldsymbol{E}_N, \boldsymbol{T}^E\right)_{\mathsf{D}} + \left(\mathcal{P}_N \boldsymbol{H} - \boldsymbol{H}_N, \boldsymbol{T}^H\right)_{\mathsf{D}} \quad ,
\end{aligned}
$$

where we have employed integration by parts once. Following the approach of Lemma 4.4 we sum over all the faces to obtain

$$
\begin{aligned}
\frac{1}{2}\frac{d}{dt}\sum_k \left((\mathcal{P}_N\boldsymbol{E}-\boldsymbol{E}_N,\varepsilon(\mathcal{P}_N\boldsymbol{E}-\boldsymbol{E}_N))_{\mathsf{D}^k}+(\mathcal{P}_N\boldsymbol{H}-\boldsymbol{H}_N,\varepsilon(\mathcal{P}_N\boldsymbol{H}-\boldsymbol{H}_N))_{\mathsf{D}^k}\right)\\
\leq -\sum_k\left[\|[\mathcal{P}_N\boldsymbol{E}-\boldsymbol{E}_N]\|^2_{\mathsf{D}^k}+\|[\mathcal{P}_N\boldsymbol{H}-\boldsymbol{H}_N]\|^2_{\mathsf{D}^k}\right]\\
+\sum_k\left[\left(\mathcal{P}_N\boldsymbol{E}-\boldsymbol{E}_N,\mathcal{P}_N\boldsymbol{T}^E\right)_{\mathsf{D}^k}+\left(\mathcal{P}_N\boldsymbol{H}-\boldsymbol{H}_N,\mathcal{P}_N\boldsymbol{T}^H\right)_{\mathsf{D}^k}\right] \quad .
\end{aligned}
$$

Note that since ε and μ are uniformly bounded away from zero the material weighted energy norm is L^2-equivalent. Furthermore, the term associated with the jump at the element interfaces is strictly negative and we recover the bound on the error

$$
\frac{1}{2}\frac{d}{dt}\sum_k\|\mathcal{P}_N\boldsymbol{q}-\boldsymbol{q}_N\|^2_{\mathsf{D}^k}\leq C\sum_k(\mathcal{P}_N\boldsymbol{q}-\boldsymbol{q}_N,\mathcal{P}_N\boldsymbol{T}^q)_{\mathsf{D}^k} \quad ,
$$

which, by using the Cauchy-Schwarz inequality and integration in time yields the result

$$
\sum_k\|\mathcal{P}_N\boldsymbol{q}(t)-\boldsymbol{q}_N(t)\|_{\mathsf{D}^k}\leq C\sum_k\left(\|\mathcal{P}_N\boldsymbol{q}(0)-\boldsymbol{q}_N(0)\|_{\mathsf{D}^k}+t\max_{s\in[0,t]}\|\mathcal{P}_N\boldsymbol{T}^q(s)\|_{\mathsf{D}^k}\right) \quad .
$$

Now combining this with Lemma 4.6 and Lemma 4.7 establishes the result and proves convergence on weak assumptions of local, elementwise smoothness of the solution. □

We have hence established the semi-discrete result that the error can not grow faster than linearly in time and that we can control the growth rate by increasing the resolution. As we shall verify in Sec. 5 this linear growth is a sharp result. However, the computations shall also verify that we can expect that the growth rate approaches zero spectrally fast when increasing the order of the approximation, n, provided the solution is sufficiently smooth.

Prior to that, a few comments are in place. A rigorous generalization of the results obtained above to cover situations with general curvilinear elements and/or spatial variation of the materials within each element is not straightforward. This is due to the generation of higher order polynomials from the products of the individual polynomial expressions of the fields, the materials and the geometry. One can, however, gain an intuitive understanding of how the geometry and material variations may impact the accuracy by assuming that the polynomial representations are not of the fields only but rather of the combined functions, $\sqrt{J}(\sqrt{\varepsilon_r}\boldsymbol{E},\sqrt{\mu_r}\boldsymbol{H})$. In this case, we are working only with n-order polynomial expansions and one can expect that the overall picture from the results derived above will hold approximately for these new functions. Hence, where we originally had an n'th order polynomial to represent the fields, $(\boldsymbol{E},\boldsymbol{H})$ we are now left with an n'th order polynomial to represent the combined variation. One consequence of this is that we loose accuracy when considering only the fields as we essentially have to share the resolution power between the fields, the geometry as well as the material variation. In particular, if the element is strongly distorted, i.e., J varies significantly, one can expect loss of accuracy as compared to the straightsided approximation. Provided, however, that the geometry is smooth, i.e., J nonsingular, and the local material variation is smooth, spectral convergence is preserved.

4.5. Convergence of Divergence Error. In the absence of sources, it is well known that the electric and the magnetic fields must remain solenoidal throughout the computation. An assumption to this effect was indeed imposed by choosing to solve only Maxwell's equations on the form Eq.(3) and considering the divergence conditions as consistency conditions on the initial conditions. However, given that we can not

expect to recover the projection of the analytic solution but rather will compute a different, albeit convergent, solution we need to consider the divergence of this numerical solution to justify the original choice of solving Eq.(3) only.

Using the results of Sec. 4.4 we can state

THEOREM 4.9. *Assume that a solution, $\boldsymbol{q} \in W^p(\mathsf{D})$, $p \geq 7/2$ to Maxwell's equations in $\Omega = \bigcup_k \mathsf{D}^k$ exists. Then there exists a constant, C, dependent on p and the angle condition of D^k, but independent of $\boldsymbol{q}$, $h = diam(\mathsf{D})$, and n, such that the divergence of the numerical solution, $\boldsymbol{q}_N$, to the semi-discrete approximation Eqs.(22)-(23) is bounded as*

$$\sum_k \|\nabla \cdot \boldsymbol{q}_N(t)\|_{\mathsf{D}^k} \leq C \sum_k \left(\frac{h^{\sigma-1}}{n^{p-1}} \|\boldsymbol{q}\|_{W^p(\mathsf{D}^k)} + t \frac{h^{\sigma-2}}{n^{p-7/2}} \max_{s\in[0,t]} \|\boldsymbol{q}(s)\|_{W^p(\mathsf{D}^k)} \right) \quad ,$$

where $\sigma = \min(p, n+1)$ and $p \geq 0$.

Proof. Considering the local divergence of $\boldsymbol{H}$ on any D we have

$$\|\nabla \cdot (\boldsymbol{H} - \boldsymbol{H}_N)\|_{\mathsf{D}} \leq \|\nabla \cdot (\boldsymbol{H} - \mathcal{P}_N \boldsymbol{H})\|_{\mathsf{D}} + \|\nabla \cdot (\mathcal{P}_N \boldsymbol{H} - \boldsymbol{H}_N)\|_{\mathsf{D}} \quad .$$

The first term we can bound immediately through Lemma 4.1 as

$$\|\nabla \cdot (\boldsymbol{H} - \mathcal{P}_N \boldsymbol{H})\|_{\mathsf{D}} \leq C \frac{h^{\sigma-1}}{n^{p-1}} \|\boldsymbol{H}\|_{W^p(\mathsf{D})} \quad ,$$

where $\sigma = \min(p, n+1)$ and $p \geq 1$.

Utilizing the inverse inequality [25]

$$\|\nabla \cdot \boldsymbol{u}_N\|_{\mathsf{D}} \leq \frac{n^2}{h} \|\boldsymbol{u}_N\|_{\mathsf{D}} \quad ,$$

for all $\boldsymbol{u}_N \in P_n^3(\mathsf{D})$, we can bound the second term as

$$\begin{aligned} \|\nabla \cdot (\mathcal{P}_N \boldsymbol{H} - \boldsymbol{H}_N)\|_{\mathsf{D}} &\leq C \frac{n^2}{h} \|\mathcal{P}_N \boldsymbol{H} - \boldsymbol{H}_N\|_{\mathsf{D}} \\ &\leq C t \frac{n^2}{h} \max_{s\in[0,t]} \left\| \mathcal{P}_N \boldsymbol{T}^H(t) \right\|_{\mathsf{D}} \\ &\leq C t \frac{h^{\sigma-2}}{n^{p-7/2}} \max_{s\in[0,t]} \left(\|\boldsymbol{E}(s)\|_{W^p(\mathsf{D})} + \|\boldsymbol{H}(s)\|_{W^p(\mathsf{D})} \right) \quad , \end{aligned}$$

by combining the results of Lemma 4.7 and Theorem 4.8. An equivalent bound can be obtained for the divergence of $\boldsymbol{E}_N$ in the case of a source free medium which, combined with the above, yields the result. □

As could be expected, the result inherits the temporal linear growth from the convergence result and confirms the possibility of recovering spectral convergence of the divergence under the assumption of sufficient smoothness of the solutions. It should be noted that while the result confirms high-order accuracy and convergence, the estimate for the actual convergence rate is almost certainly suboptimal and leaves room for improvement.

4.6. Entr'acte on the Scattered Field Formulation. Let us briefly return to an analysis of the scattered field formulation discussed in Sec. 2.1, with the modified scattered field equations given in Eqs.(7)-(8). We recall that we split the solution, $\boldsymbol{q}$, as

$$\boldsymbol{q} = \boldsymbol{q}^s + \boldsymbol{q}^i \quad ,$$

and exploit the linearity of Maxwell's equations to solve for the scattered field, $\boldsymbol{q}^s$, subject to the forcing by the incident field, $\boldsymbol{q}^i$. As discussed in Sec. 2.1, this does not alter the scheme in any significant way except at metallic boundaries where the boundary condition on the electric field component takes the form

$$\boldsymbol{n} \times \boldsymbol{E}_N^{s,+} = -\boldsymbol{n} \times \boldsymbol{E}_N^{s,-} - 2\mathcal{P}_N \boldsymbol{E}^i \quad ,$$

in the notation of Lemma 4.4, while the boundary condition on the magnetic field remains

$$\boldsymbol{n} \times \boldsymbol{H}_N^{s,+} = \boldsymbol{n} \times \boldsymbol{H}_N^{s,-} \quad .$$

Since this constitutes the only difference, we can restrict the subsequent analysis to the case of a metallic object in vacuum without loss of generality as all other complications are covered by the analysis of the total field scheme.

It suffices to consider the behavior of the computed solution which can be bounded as stated in the following.

THEOREM 4.10. *Assume that a scattered field solution, $\boldsymbol{q}^s \in W^p(\mathsf{D})$, $p \geq 3/2$ to Maxwell's equations in $\Omega = \bigcup_k \mathsf{D}^k$ exists, and that the incident field $\boldsymbol{q}^i \in W^p(\mathsf{D})$, $p \geq 3/2$. Then the energy of the numerical scattered field solution, $\boldsymbol{q}_N^s$, to the semi-discrete approximation of Eqs.(7)-(7) is bounded as*

$$\begin{aligned}\sum_k \|\boldsymbol{q}_N^s(t)\|_{\mathsf{D}^k} \leq & C \sum_k \Big(\left\|\mathcal{P}_N \boldsymbol{q}^i(t)\right\|_{\mathsf{D}^k} \\ & + \left\|\mathcal{P}_N \boldsymbol{q}^i(0) + \boldsymbol{q}_N^s(0)\right\|_{\mathsf{D}^k} + t \max_{s\in[0,t]} \left\|\boldsymbol{T}^{q,i}(s)\right\|_{\mathsf{D}^k} \Big) \quad ,\end{aligned}$$

where C depends on the material properties and the angle conditions of the elements but not on h and n.

Proof. The proof proceeds in a way very similar to that of Theorem 4.8. Combining the equation for the scattered field solution, $\boldsymbol{q}_N^s$, with the equation describing the projection of the incident field, $\mathcal{P}_N \boldsymbol{q}^i$, summing over all the faces and using $\boldsymbol{q}_N^s + \mathcal{P}_N \boldsymbol{q}^i$ as the test function we recover

$$\begin{aligned}\frac{1}{2}\frac{d}{dt} \sum_k \left\|\boldsymbol{q}_N^s + \mathcal{P}_N \boldsymbol{q}^i\right\|_{\mathsf{D}^k}^2 \leq & - \sum_{\text{Interior Faces}} \left\|[\mathcal{P}_N \boldsymbol{q}^i + \boldsymbol{q}_N^s]\right\|_{\mathsf{D}^k}^2 \\ & -4 \sum_{\text{PEC Faces}} \left\|[\mathcal{P}_N \boldsymbol{E}^i + \boldsymbol{E}_N^s]\right\|_{\mathsf{D}^k}^2 \\ & + \sum_k \left(\mathcal{P}_N \boldsymbol{q}^i + \boldsymbol{q}_N^s, \mathcal{P}_N \boldsymbol{T}^{q,i}\right)_{\mathsf{D}^k} \quad ,\end{aligned}$$

where the dissipative terms are gathered over the interior and PEC faces separately due to different boundary conditions, while the global sum involves the truncation error, $\mathcal{P}_N \boldsymbol{T}^{q,i}$, associated with the projection of the incident field.

This latter term can be bounded as in Lemma 4.7

$$\left\|\mathcal{P}_N \boldsymbol{T}^{q,i}\right\|_{\mathsf{D}} \leq C \frac{h^{\sigma-1}}{n^{p-3/2}} \left\|\boldsymbol{q}^i\right\|_{W^p(\mathsf{D})} \quad ,$$

where $\sigma = \min(p, n+1)$.

Proceeding as for Theorem 4.8 we subsequently recover

$$\sum_k \left\| \boldsymbol{q}_N^s(t) + \mathcal{P}_N \boldsymbol{q}^i(t) \right\|_{\mathsf{D}^k} \leq C \sum_k \left\| \boldsymbol{q}_N^s(0) + \mathcal{P}_N \boldsymbol{q}^i(0) \right\|_{\mathsf{D}^k} + t \max_{s\in[0,t]} \sum_k \left\| \mathcal{P}_N \boldsymbol{T}^{q,i}(s) \right\|_{\mathsf{D}^k} \quad ,$$

from which

$$\sum_k \left\| \boldsymbol{q}_N^s(t) \right\|_{\mathsf{D}^k} \leq C \sum_k \left\| \mathcal{P}_N \boldsymbol{q}^i(t) \right\|_{\mathsf{D}^k} + \sum_k \left\| \boldsymbol{q}_N^s(0) + \mathcal{P}_N \boldsymbol{q}^i(0) \right\|_{\mathsf{D}^k} + t \max_{s\in[0,t]} \sum_k \left\| \mathcal{P}_N \boldsymbol{T}^{q,i}(s) \right\|_{\mathsf{D}^k} \quad ,$$

thus establishing the result. □

Hence, also the scattered fields remain bounded up to linear growth in time. An interesting difference between this result on that of Theorem 4.8 for the total field formulation is that the accuracy and growth rate of the former is controlled solely by the smoothness of the incident field with the potential for exponential convergence for sufficiently smooth illuminating fields.

5. Validation and Performance of the Scheme. Having developed the complete formulation for the time-domain solution of Maxwell equations, supported by a thorough convergence analysis, it is now time to consider the actual performance of the computational framework.

In the following we shall discuss the validity of the main theoretical results through a few examples as well as exemplify the versatility and overall accuracy and performance of the complete framework for a number of benchmarks. Temporal integration of the semi-discrete approximation given in Eqs.(20)-(21) is done using a 4th order, 5 stage low-storage Runge-Kutta scheme [36] and a stability limited time-step scaling as

$$\Delta t \leq \mathrm{CFL} \min_{\Omega} \sqrt{\varepsilon_r \mu_r} |\boldsymbol{\chi}|^{-1} \quad ,$$

with $\sqrt{\varepsilon_r \mu_r}$ reflecting the modified local speed of light due to materials and

$$\boldsymbol{\chi} = \frac{|\nabla \xi|}{\Delta \xi} + \frac{|\nabla \eta|}{\Delta \eta} + \frac{|\nabla \zeta|}{\Delta \zeta} \quad .$$

Here $|\cdot|$ refers to the absolute value of each and of the vector components, i.e., $|\nabla \xi| = [|\xi_x|, |\xi_y|, |\xi_z|]^T$. Hence, $\boldsymbol{\chi}$ provides a measure of the local grid-distortion as a consequence of the mapping, Ψ, of I into D, and $(\Delta\xi, \Delta\eta, \Delta\zeta)$ measures axial distance separating neighboring nodal points in I. In this setting CFL typically takes values of $\mathcal{O}(1)$ while the time step, Δt, scales as $\Delta t \simeq l/n^2$ where l is the minimum edge length on all tetrahedra and n is the polynomial order of the approximation.

As a general measure of error we shall use the discrete L^p-norm of the error defined as

$$\|\delta f(t)\|_p = \left(\sum_{j,k} \left[f_N(\boldsymbol{x}_j^k, t) - f(\boldsymbol{x}_j^k, t) \right]^p \right)^{1/p} \quad ,$$

where $f_N(\boldsymbol{x}, t)$ is the numerical approximation to the exact value, $f(\boldsymbol{x}, t)$ summed over all nodes, j, within each of the k elements.

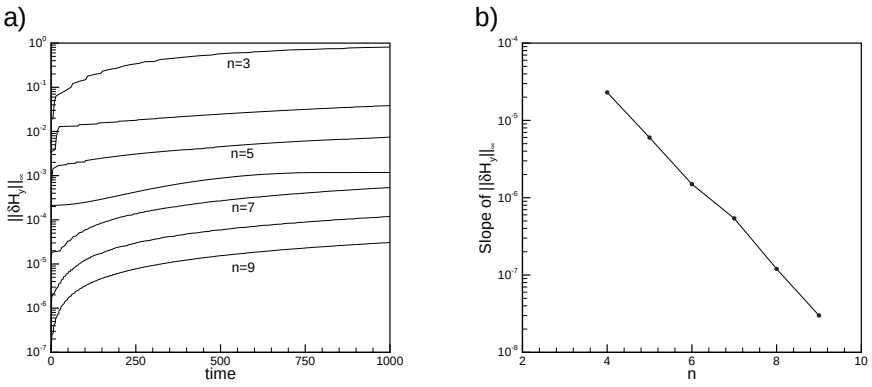

FIG. 3. *In a) is shown the temporal envelope of the maximum error on $H_y(t)$ in the two-dimensional cavity for different orders, n, of the approximation. The slope of the linear growth is plotted in b), confirming spectral convergence as predicted in Theorem 4.8.*

5.1. Elementary Tests and Verification of Theoretical Results. As a first verification of the theoretical estimates, and in particular the linear growth predicted in Theorem 4.8, we consider the solution of the two-dimensional Maxwell's equations in the TM-polarization, i.e., we solve for (H_x, H_y, E_z). There is, however, nothing special about this polarization.

The computational problem is that of a simple two-dimensional vacuum filled cavity, assumed to be defined by $(x, y) \in [-1, 1] \times [-0.25, 0.25]$, with the walls at $x = \pm 1$ taken to be perfect electrical conducts while the cavity is assumed to be periodic in the y-direction. The initial condition is a simple oscillatory cavity solution as

$$H_x(x, y, 0) = 0 \ , \ \ H_y(x, y, 0) = \cos(\pi x) \ , \ \ E_z(x, y, 0) = 0 \ ,$$

and the computational domain is discretized by 8 equivalent isosceles, each with 0.5 wavelength long sides.

In Fig. 3 we show the temporal envelope of the maximum error of $H_y(t)$, computed using the same eight elements while increasing the order of the approximation. Following the main result, Theorem 4.8, we expect that the error can grow at most linearly in time and that the growth rate should vanish spectrally for smooth solution. The results in Fig. 3 not only confirm the validity of both statements but also illustrates that Theorem 4.8 is sharp, i.e., we can not in general guarantee slower than linear error growth, although we can control the growth rate by the order of the approximation.

To further evaluate the performance of the scheme, let us briefly consider the behavior of the divergence and the ability of the scheme to propagate waves over long distances. For this purpose we shall continue to consider the propagation of plane waves in simple rectangular domains, tiled using isosceles, each with an edge length of 0.5 wavelength. In Fig. 4 we show the global L^2-error of the divergence of $\boldsymbol{H}$ for a plane wave propagating in a fully periodic domain being 2 wavelengths long and 0.5 wavelength wide, tiled using only 8 triangles. Consistent with the theoretical result in Theorem 4.9 the scheme preserves the divergence error to the order of the scheme, i.e., the error vanishes spectrally as we refine the order, n, of the approximation. The very notable even-odd behavior in the convergence is a consequence of the alignment with the triangulation.

The ability to propagate waves over very long distances is likewise illustrated in Fig. 4 where we also show the L^2-error of the H_y component. Contrary to the small problems considered first, we are here considering a 200 wavelength long domain and with the exact solution being use to truncate the computational domain. The domain is tiled using isosceles with an edge length of 0.5 wavelength and a total of 800 elements. We

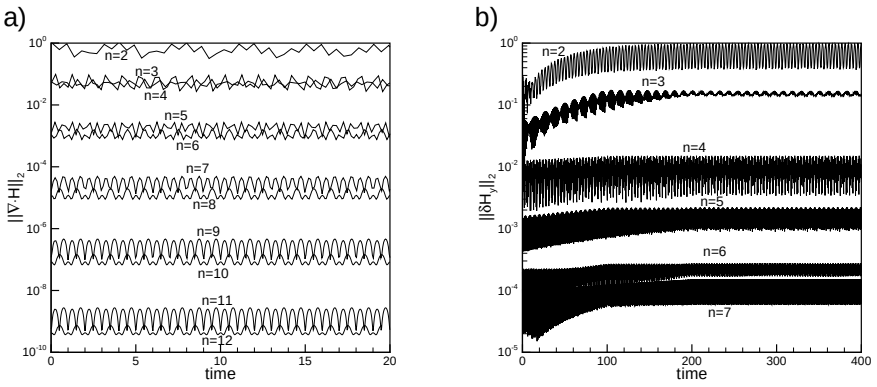

FIG. 4. *In a) is shown the global L^2-error of the divergence of $\boldsymbol{H}$ for a plane wave propagating in a fully periodic domain as a function of time and order of approximation, n, confirming that the scheme conserves divergence to the order of the approximation, i.e., it decays spectrally with increasing polynomial order. The L^2-error of H_y as a function of time and order of approximation, n, in a 200 wavelength long domain is shown in b), confirming the ability to propagate waves over very long periods of time using only few points per wavelength.*

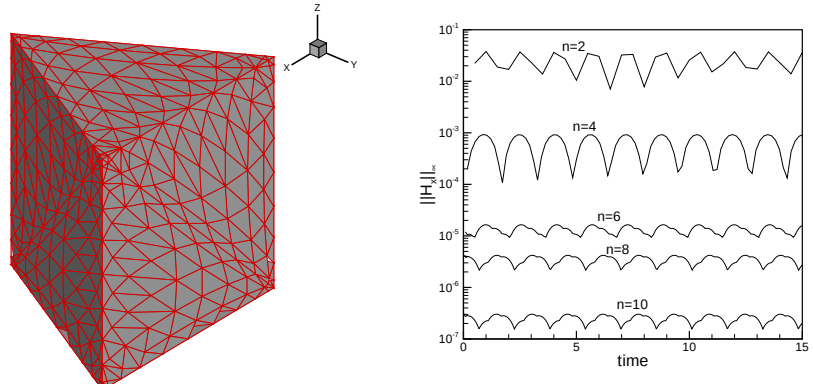

FIG. 5. *In a) we illustrate the prism tiled using three high-order tetrahedra while b) illustrates the maximum of H_x for a (y,z)-polarized plane wave propagation as a function of time and order of the approximation, n, confirming spectral convergence for the three-dimensional case.*

observe in Fig. 4 an expected slow error growth until $t = 200$ after which it settles at a maximum error level. This level, however, decays spectrally as we increase the order, n, of the approximation. Using as a guideline that two edges span a wavelength, we see that with 7 points per wavelength (two $n = 3$ triangles) yields about 10% error, only 9 points per wavelength (two $n = 4$ triangles) results in about 1% error while 11 points per wavelength (two $n = 5$ triangles) ensures about 0.1% error after 400 periods. This is a testament to the advantage of using a high-order framework for wave propagation problems.

Let us finally consider a simple three-dimensional test case in which we have tiled a straightfaced prism using three straightfaced tetrahedra as illustrated in Fig. 5. The test is that of a plane wave propagating through the prism with the exact solution being used as the boundary conditions. As shown in Fig. 5 we recover a rapid exponential convergence as the order, n, of the approximation is increased.

5.2. Two-Dimensional Examples. Having verified the performance of the basic computational setup as well as the theoretical estimates, let us now consider problems of a less simple and more realistic character. This shall not only allow us to illustrate more general features of the proposed framework but shall also be

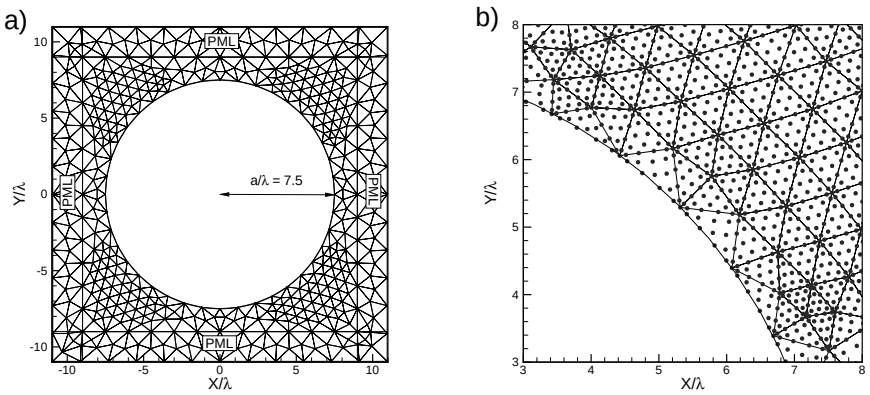

FIG. 6. *In a) is shown the finite element grid, consisting of 854 triangles, used for computing scattering by a perfect electrically conducting cylinder of size $ka = 15\pi$. A section of the grid in b) illustrates the bodyconforming nature of the grid and the nodal grid supporting the high-order approximation.*

used to verify that all the properties of the high-order unstructured grid approach, seen so convincingly in the last section for simple examples, carry over to the solution of more realistic problems.

We shall focus the attention on problems described by the two-dimensional TM-polarized Maxwell's equations on the form

$$
\begin{aligned}
\mu_r \frac{\partial H_x}{\partial t} &= -\frac{\partial E_z}{\partial y} \ , \\
\mu_r \frac{\partial H_y}{\partial t} &= \ \ \frac{\partial E_z}{\partial x} \ , \\
\varepsilon_r \frac{\partial E_z}{\partial t} &= \ \ \frac{\partial H_y}{\partial x} - \frac{\partial H_x}{\partial y} \ ,
\end{aligned}
\tag{31}
$$

subject to boundary conditions between two regions with material parameters, $\varepsilon_r^{(k)}$ and $\mu_r^{(k)}$, for $k = 1, 2$, as

$$
\begin{aligned}
\hat{\boldsymbol{n}} \times \boldsymbol{H}^{(1)} &= \hat{\boldsymbol{n}} \times \boldsymbol{H}^{(2)} \ , \\
E_z^{(1)} &= E_z^{(2)} \ .
\end{aligned}
$$

Here $\boldsymbol{H}^{(k)} = (H_x^{(k)}, H_y^{(k)}, 0)^T$ and $\hat{\boldsymbol{n}} = (\hat{n}_x, \hat{n}_y, 0)^T$ represents a unit vector normal to the interface. For the case of a perfectly conducting metallic boundary the condition becomes particularly simple as

$$
E_z = 0 \ .
$$

The computational domain is truncated with a Cartesian PML [37] using a quadratic absorption profile.

It is worthwhile emphasizing that results of equal quality and overall accuracy as the ones shown in the following for the TM-polarized case has been obtained for the TE-polarized case.

As a first example we consider that of plane wave scattering by a perfectly conducting circular cylinder with a radius of $a = 7.5\lambda$, i.e., $ka = 15\pi$. The surrounding medium is assumed to be vacuum, i.e., $\varepsilon_r = \mu_r = 1$. The finite element grid, consisting of 854 triangles, utilized for this computation is shown in Fig. 6 along with a section of the grid illustrating the full bodyconforming nature of the approximation as well as the nodal grid supporting the high-order approximation. Maxwell's equations are solved in the scattered field formulation

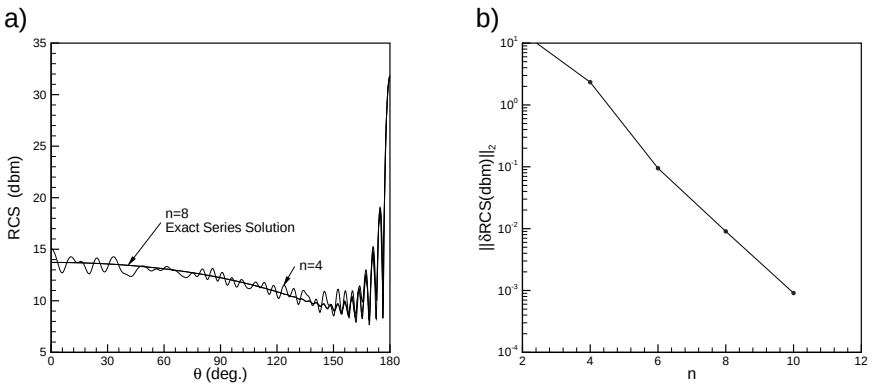

FIG. 7. *In a) is shown the bistatic radar cross section, RCS(θ), as computed using the exact series representation as well as the unstructured grid method at different polynomial orders, n. Evidence of high-order convergence for the RCS-computation is given in b) showing exponential decay of the error in RCS(dBm) with increasing order of the approximation.*

and Prony extrapolation [38] is used to reduce the required computing time to reach the harmonic steady state.

In Fig. 7 we compare the computed bistatic radar cross section, RCS(θ), with the exact series solution [39], for various orders, n, of the approximation using the finite element grid illustrated in Fig. 6. As expected we observe a very rapid convergence with increasing n, yielding a reasonable engineering accuracy computation with the 4th order scheme while increasing the order to $n = 8$ results in a perfect match. A quantitative confirmation of this is also shown in Fig. 7, illustrating the expected exponential convergence of the RCS with increasing n.

One of the most appealing advantages of a high-order framework on simplices is the ability to import a strongly skewed finite element grid and recover a fully converged solution by increasing the order of the approximation rather than having to reconstruct an improved finite element discretization. This property is particularly important and useful for large three-dimensional problems where the grid generation phase can be very complex and time-consuming. As an illustration of this approach to convergence, we consider in Fig. 8 the plane wave scattering from a PEC cylinder with a radius of one wavelength, i.e., $ka = 2\pi$. The measure of accuracy and convergence is based on the observation that the symmetry of the problem makes one expect the scattered fields themselves maintain a high degree symmetry.

This is indeed confirmed in Fig. 8 where we show a deliberately chosen poor grid and the rapid recovery of the symmetry of one of the scattered field components, H_x, as the order, n, of the approximation is increased without modifying the underlying finite element grid. The detail to which the symmetry is restored is particularly noteworthy.

As an illustration of the capability to handle materials let us consider plane wave scattering by a penetrable circular cylinder with a radius of $a = 3.5\lambda$ consisting of an ideal dielectric with $\varepsilon_r = 2.0$, i.e., similar to that of glass. The problem is again solved in a pure scattered field formulation and the fully body-conforming finite element discretization, consisting of a total of 1020 triangles, is illustrated in Fig. 9. We note that the absorbing PML layer, containing about 2/3 of the total amount of triangles is unnecessarily thick for illustration only and can be decreased without loss of accuracy.

As is likewise illustrated in Fig. 9 we recover the full bistatic radar cross section, RCS(θ), with excellent correspondence to the exact solution [40] and quantitative agreement over a 40 db dynamic range.

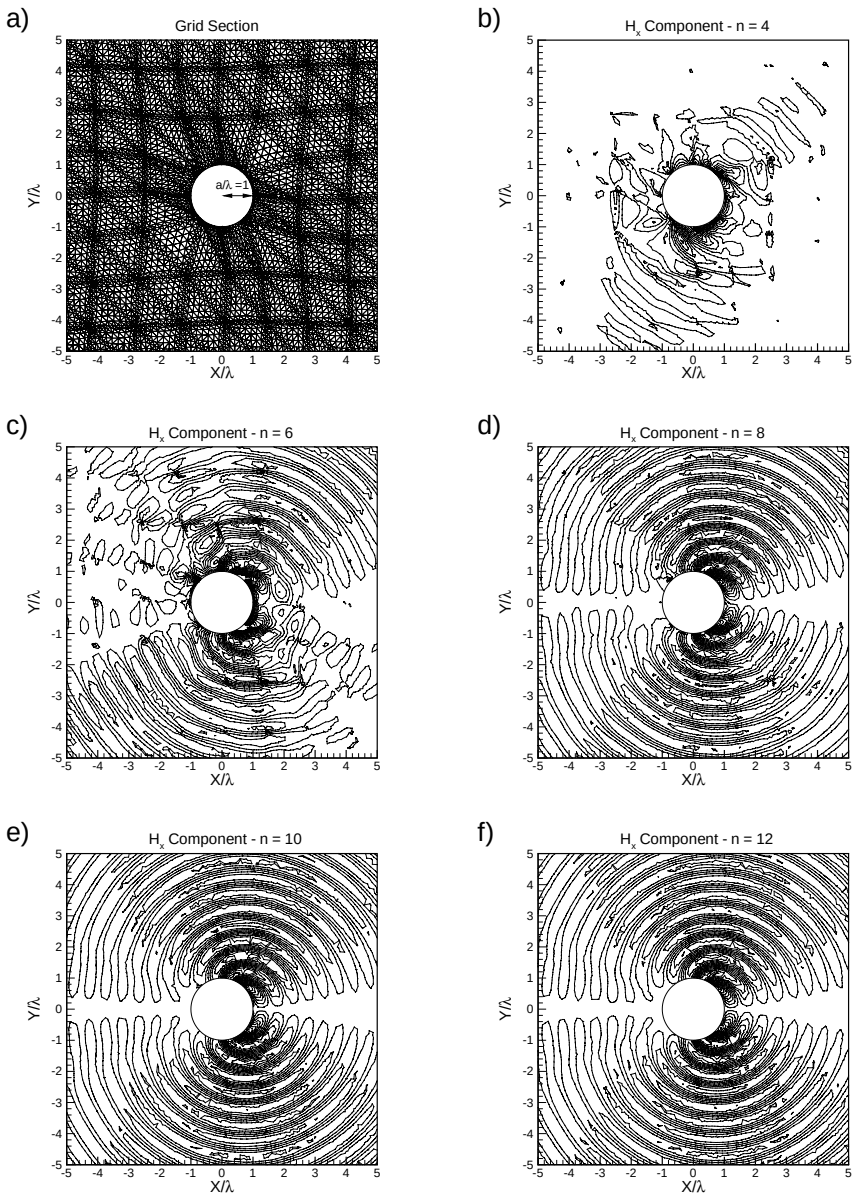

FIG. 8. *Example of convergence by increasing the order of the approximation, n, on a deliberately chosen highly skewed finite element grid, illustrated in a). The convergence is illustrated in b)-f) for increasing the order from 4'th order to 12'th order, showing a complete recovery of the expected symmetry of the scattered field component,* H_x.

5.3. Three-Dimensional Examples. As a first verification of the general three-dimensional framework, let us consider plane wave scattering by a $ka = 10$ perfectly conducting sphere, the analytic solution of which is given by a Mie-series [39].

We use a fully bodyconforming grid with a total of 3000 elements, having an average edge length at the sphere of $4\lambda/5$. Contrary to the two-dimensional case where we used a PML to truncate the computational domain we choose in the three-dimensional case to embed the sphere in a $(20\lambda)^3$ cube and employ stretching of the elements as one approaches the outer boundary. The grid is stretched such that the average edge is about 2λ at the outer boundary. As in the two-dimensional case, all examples are done using a 4th order

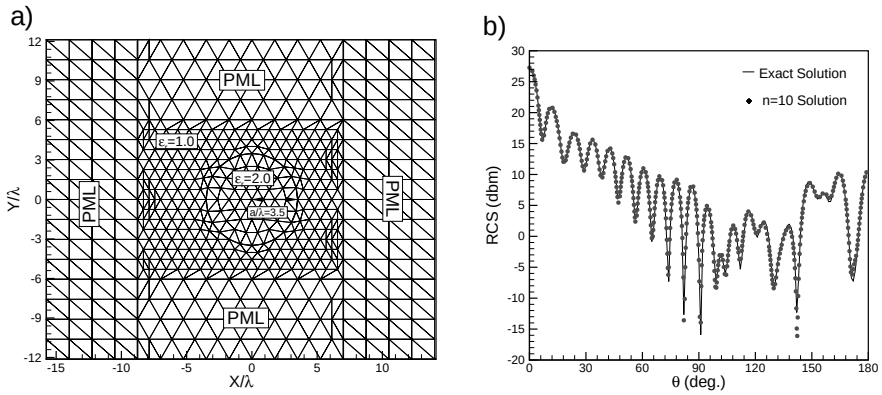

FIG. 9. *Plane wave scattering by a $ka = 7\pi$ dielectric circular cylinder with a relative permittivity $\varepsilon_r = 2.0$. In a) we show the finite element discretization while b) shows a comparison between the computed bistatic radar cross section, RCS(θ), obtained with a 10'th order approximation and that recovered by evaluating the exact solution.*

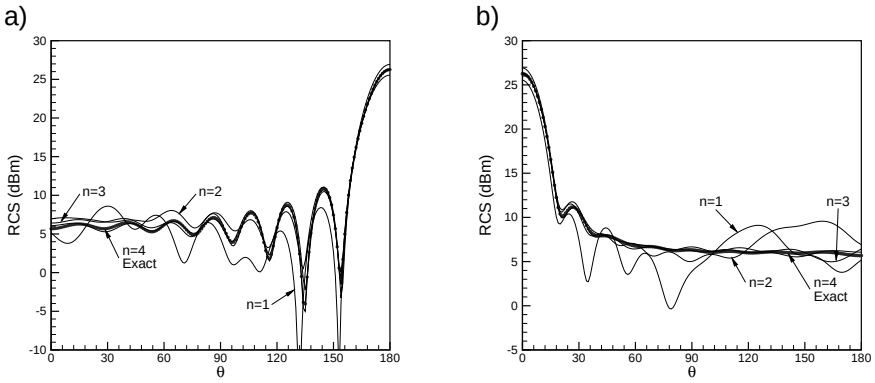

FIG. 10. *Plane wave scattering by a $ka = 10$ metallic sphere for a fixed grid and increasing order, n, of the polynomial approximation. In a) we show the convergence of RCS(θ,0) for vertical polarization (TM), while b) shows RCS(θ,90) for horizontal polarization (TE) of the incident field.*

low-storage Runge-Kutta scheme to advance in time and Prony extrapolation to identify the solution.

In Fig. 10 we illustrate the convergence of the scheme with a fixed grid when increasing the order of the approximation within each tetrahedron. Even for $n = 3$, i.e., a third order scheme with about 5 points per wavelength, do we compute a reasonable solution while increasing the order yields a rapidly converging solution as one would expect.

As a considerably more challenging problem, let us consider scattering by a perfectly conducting business card sized metallic plate as illustrated in Fig. 11. The horizontally polarized plane wave impinges at the metallic plate at an almost grazing angle, causing the excitation of very strong waves along the edges of the metallic plate. These waves contribute dramatically to the scattering process and need to be resolved to accurately predict the far field scattering.

This problem, being one of the EMCC benchmark problems [41] for code validation, is addressed by using a total of 27000 straightsided tetrahedra, each supporting a 4th order polynomial approximation. The average edge length at the edge of the business card is approximately $\lambda/5$. The metallic plate is embedded in a $(20\lambda)^3$ cube, with the elements being stretched to about 4λ at the outer boundary.

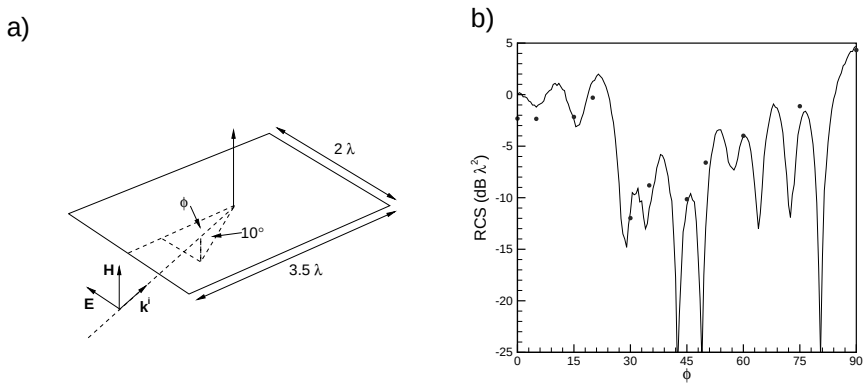

FIG. 11. *In a) we show the geometry for the plane wave scattering by a metallic business card while b) shows the comparison between monostatic RCS experimental results [41] (full line) for horizontal polarization of the illuminating field and particular computed data points (·).*

In Fig. 11 we also show the comparison between the experimentally measured monostatic RCS [41] and a number of particular computed data points. Again we observe good agreement over the full azimuthal range with results well within the experimental error. The most significant discrepancy of a few dB for $\phi \sim 0$ is consistent with other published results [41].

As a final example of the performance of the three-dimensional framework we shall consider plane wave scattering from a dielectric cylinder of finite length. As illustrated in Fig. 12, the length of the cylinder is 5λ and the non-magnetic material has a permittivity of $\varepsilon_r = 2.25$, similar to that of glass. Clearly, the nature of the fields is less dramatic than in the previous case and we find that using a total of approximately 67000 elements, supporting a 4th order approximation and with an average vacuum edge length at the cylinder of $\lambda/3$, suffices to accurately predict the far field scattering. The full computational domain is a cylinder of radius 16λ and length 23λ with the stretched elements having a average length of 4λ at the outer boundary.

In Fig. 12 we show a direct comparison between the full bistatic RCS for a plane wave impinging directly at the end of the cylinder as computed using the current framework as well as an independently verified pseudospectral multi-domain axi-symmetric code [12]. As expected we find an almost perfect agreement between the results of the two schemes over approximately 50 dB dynamical range.

5.4. Parallel Performance. The discontinuous element formulation of the scheme enables a highly efficient implementation at contemporary large scale distributed memory machines. While this is a lesser concern for the two-dimensional schemes, it is essential to enable the modeling of large scale three-dimensional problems.

The developed schemes are implemented in a combination of Fortran and C with all computationally intensive part written in Fortran and taking advantage of Level 3 BLAS [42] where possible. The parallel interface is written in MPI [43] with METIS [44] used to distribute the elements over the processors. To ensure high cache efficiency, we employ bandwidth minimization [45] of the nodal points locally to the processors [46]. For computations maximizing the capacity of the processors, i.e., filling the local memory, this is critical to ensure high performance.

In Table 1 we list the parallel speedup relative to the $n = 2$ case as the number of processors are increased. A few things are worth noting. For a fixed size problem, the parallel speedup decreases slightly as the number of processors increases which is natural as the relative communication cost increases. On

TABLE 1

Parallel speedup for a 123.000 element grid, scaled to timing for $n = 2$ on 4 processors (- implies insufficient memory local to the nodes).

Polynomial order (n)	Degrees of freedom ($\times 10^6$)	Number of processors				
		4	8	16	32	64
2	7.4	1.0	2.0	3.9	7.5	13.7
3	14.8	-	0.9	1.8	3.5	6.4
4	25.8	-	-	1.0	1.9	3.6
5	41.3	-	-	-	0.8	1.6

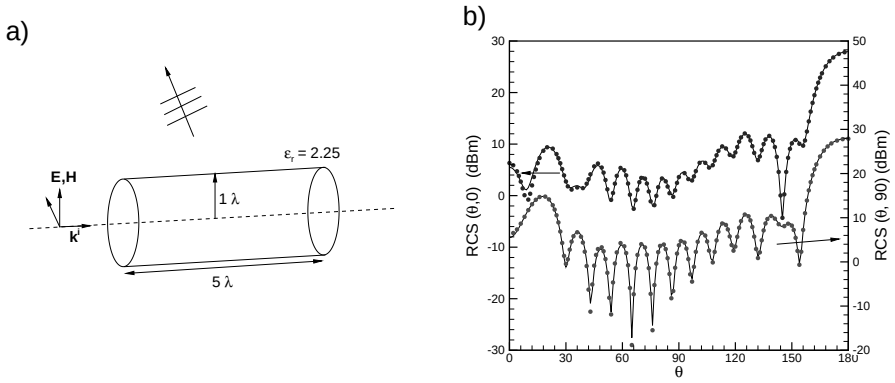

FIG. 12. *In a) we show the geometry for the plane wave scattering by a dielectric finite length cylinder while b) shows the RCS(θ,0) for vertical polarization (·) of the illuminating field and RCS(θ,90) for horizontal polarization (·) compared with results obtained using a pseudospectral axi-symmetric code (full line) [12]*

the other hand, for problem sizes utilizing the available resources we find a very high parallel efficiency, e.g., increasing the problem size and the number of processors yields a close to constant speedup. The data also show a minor decrease in relative performance for high order on many processors, which we speculate is related to cache effects known to be become important as the size of the operators increase [29]. We generally observe better than 90% parallel efficiency, consistent with other similar studies [47].

6. Concluding Remarks and Outlook. The main purpose of paper has been to introduce the reader to a new class of high order unstructured grid methods suitable for the time-domain solution of Maxwell's equations. A number of central elements separate the current framework from previous attempts to develop high-order accurate methods on unstructured grids. The use of a purely nodal basis has a number of advantages in terms of ease of implementation by simple matrix-vector operations as well as the promise to yield a highly efficient implementation. Furthermore, the generalized discontinuous penalty scheme was introduced, offering an inherently parallel discontinuous formulation with a purely block-diagonal mass matrix which can be inverted in preprocessing.

The particular focus on Maxwell's equations allowed us to develop a complete, if not optimal, convergence theory. A similar analysis can be completed for other classes of linear problems such as acoustics and linear elasticity. We have confirmed the results of the analysis by thorough computational experiments, illustrating the flexibility, versatility, and efficiency of the proposed high-order accurate unstructured grid framework.

While we have focused on linear systems in general and Maxwell's equations in particular, the central elements of the framework allows for more general formulations that enable the solution of typical nonlinear

systems of conservation laws. This naturally raises questions about proper formulation of the fluxes at interfaces, conservation, entropy solutions and stability of high-order schemes when approximating problems with discontinuous solutions. We shall address these issues in [30] where we shall also demonstrate the performance of such generalized formulations for the solution of conservation laws.

Acknowledgment. The authors extend their appreciation to Prof. D. Gottlieb and Dr. A. Ditkowski, Brown University, for many fruitful discussions.

Efficient and Accurate Implementation Techniques. From the discussions in Sec. 3.2 it is clear that the Vandermonde matrix, V, plays a crucial role in setting up the discrete operators for interpolation and differentiation. The properties of V, e.g., its conditioning, depends exclusively on the structure of nodal set, $\boldsymbol{\xi}_j$, and on the way in which we choose to represent the basis, i.e., $p_i(\boldsymbol{\xi})$. While the former is chosen to ensure well behaved Lagrange interpolation polynomials, we have significant freedom in the specification of $p_i(\boldsymbol{\xi})$.

A particularly simple choice is that of the multivariate monomial basis, i.e., $p_i(\boldsymbol{\xi}) = \xi^i \eta^j \zeta^k$. However, even for interpolation in one dimension, i.e., $p_i(\xi) = \xi^i$, is it well known that this basis leads to the classical Vandermonde matrix with an exponentially growing condition number. Hence, even for moderate values of n can we expect severe problems when attempting to compute the action of V^{-1}. The well known solution to this problem is to choose a basis that is orthonormalized with respect to some proper inner product to assure the maximum degree of linear independence of the basis.

Such a basis has been known for long [48, 49, 50] and takes the form

$$\psi_{ijk}(\boldsymbol{\xi}) = P_i^{(0,0)}(r) \left(\frac{1-s}{2}\right)^i P_j^{(2i+1,0)}(s) \left(\frac{1-t}{2}\right)^{i+j} P_k^{(2i+2j+1,0)}(t) \quad , \tag{32}$$

where

$$r = -\frac{2(1+\xi)}{\eta+\zeta} - 1 \quad , \quad s = \frac{2(1+\eta)}{1-\zeta} - 1 \quad , \quad t = \zeta \quad ,$$

and $P_n^{(\alpha,\beta)}(x)$ signifies the classical Jacobi polynomial of order n [51].

The tensor product structure of the basis, Eq.(32), becomes evident when one realizes that while $\boldsymbol{\xi}$ is restricted by I, the mapped coordinates, (r, s, t), covers $[-1, 1]^3$. Furthermore, it is easy to see that the polynomial space P_n^3 can expressed as

$$\mathsf{P}_n^3 = \mathrm{span}\left\{\psi_{ijk}(\boldsymbol{\xi}); i, j, k \geq 0; i + j + k \leq n\right\} \quad .$$

An important property of the basis, Eq.(32), is its orthogonality on I [21] as

$$\int_{\mathsf{I}} \psi_{ijk}(\boldsymbol{\xi}) \psi_{pqr}(\boldsymbol{\xi}) \, d\boldsymbol{\xi} = \gamma_{ijk} \delta_{ijk,pqr} \quad ,$$

where $\delta_{ijk,pqr}$ is the multi-dimensional Dirac delta and the normalization is

$$\gamma_{ijk} = \frac{2}{2i+1} \frac{2^{2i+2}}{2(i+j)+2} \frac{2^{2(i+j)+3}}{2(i+j+k)+3} \quad .$$

Let us introduce the index, $\alpha \in [0, N]$, reflecting some chosen ordering of (i, j, k) and hence ψ_{ijk}. We can thus rename the polynomial basis $\psi_{ijk}(\boldsymbol{\xi}) = \psi_\alpha(\boldsymbol{\xi})$ to simplify the notation in the subsequent discussion.

With this machinery in place, let us address how to initialize the basic operations and the associated operators needed for solving partial differential equations with the current context in an efficient and accurate manner.

Using the orthogonal basis, ψ_α, it is natural to define the Vandermonde matrix to have the entries

$$\mathrm{V}_{ij} = \frac{1}{\sqrt{\gamma_j}} \psi_j(\boldsymbol{\xi}_i) \quad .$$

The relation between the nodal and the modal representation of a function, f, follows directly from Eq.(12) as

$$\boldsymbol{f} = \mathrm{V}\hat{\boldsymbol{f}} \quad , \quad \hat{\boldsymbol{f}} = \mathrm{V}^{-1}\boldsymbol{f} \quad .$$

Furthermore, we can compute the entries of the differentiation matrices directly by defining the entries of $\mathrm{P}^{(\xi,\eta,\zeta)}$, Eq.(15), using the derivatives of $\psi_i(\boldsymbol{\xi})$ expressed explicitly by the identity [51]

$$\frac{d}{d\xi} P_n^{(\alpha,0)}(\xi) = \frac{1}{2}(n+1+\alpha) P_{n-1}^{(\alpha+1,1)}(\xi) \quad .$$

In an equally simple and straightforward way we can define spatial filtering matrices, F, as

$$\mathrm{F} = \mathrm{V}\sigma(i,j,k)\mathrm{V}^{-1} \quad ,$$

where the order p filter itself is defined as

$$\sigma(i,j,k) = \exp\left[-\alpha\left(\frac{(i+j+k)(i+j+k+3)}{n}\right)^p\right] \quad ,$$

such that filtering is accomplished through a straightforward matrix multiply at a cost equivalent to that of computing a spatial derivative.

While the interpolation, differentiation, and filtering operators will play a crucial role in the solution of the partial differential equations, we shall also need to evaluate inner products on the general curvilinear tetrahedron, i.e., we shall need an efficient and accurate procedure for computing

$$(f_N, g_N)_{\mathsf{D}} = \int_{\mathsf{I}} f_N(\boldsymbol{\xi}) g_N(\boldsymbol{\xi}) J(\boldsymbol{\xi}) d\boldsymbol{\xi} \quad ,$$

where J refers to the transformation Jacobian for the mapping between D and I and $f_N \in P_n^3$, $g_N \in P_n^3$. To evaluate this inner product, we exploit that f_N and g_N are expressed uniquely by their expansion in Lagrange polynomials as

$$(f_N, g_N)_{\mathsf{D}} = \sum_{i,j=0}^{N} f_i g_j \int_{\mathsf{I}} L_i(\boldsymbol{\xi})\, L_j(\boldsymbol{\xi})\, J(\boldsymbol{\xi})\, d\boldsymbol{\xi} \quad .$$

Furthermore, using the basis itself, $\psi_\alpha(\boldsymbol{\xi})$, we can express the Lagrange polynomials themselves using Eq.(14) on the form

$$L_i(\boldsymbol{\xi}) = \sum_{k=0}^{N} \mathrm{V}_{ik}^{-1} \psi_k(\boldsymbol{\xi}) \quad .$$

This immediately yields the expression

$$(f_N, g_N)_{\mathsf{D}} = \sum_{i,j=0}^{N} f_i g_j \sum_{k,l=0}^{N} \mathrm{V}_{ki}^{-1} \mathrm{V}_{lj}^{-1} \int_{\mathsf{I}} \psi_k(\boldsymbol{\xi}) \psi_l(\boldsymbol{\xi}) J(\boldsymbol{\xi})\, d\boldsymbol{\xi} \tag{33}$$
$$= \sum_{i,j=0}^{N} f_i g_j \sum_{k,l=0}^{N} \mathrm{V}_{ki}^{-1} \mathrm{V}_{lj}^{-1} \mathrm{W}_{kl} \quad ,$$

where the symmetric matrix of weights, W, has the entries

$$\mathrm{W}_{kl} = \int_{\mathsf{I}} \psi_k(\boldsymbol{\xi}) \psi_l(\boldsymbol{\xi}) J(\boldsymbol{\xi})\, d\boldsymbol{\xi} \quad .$$

On matrix form Eq.(33) becomes

$$(f_N, g_N)_{\mathsf{D}} = \left(\mathrm{V}^{-1} \boldsymbol{f}\right)^T \mathrm{W} \mathrm{V}^{-1} \boldsymbol{g} \quad .$$

For all elements we may precompute $(\mathrm{V}^{-1})^T \mathrm{W} \mathrm{V}^{-1}$ in a preprocessing stage, storing only the upper half of the operator due to symmetry. In the particularly important case where D is a straightsided tetrahedron, i.e., J is a constant, the orthonormality of ψ_α implies that $\mathrm{W} = J\mathrm{I}$, where I represents the identity matrix. Hence, through a simple linear scaling one recovers the weights for all tetrahedra with planar faces. For the general case where $J(\boldsymbol{\xi})$ is non constant, the entries of W are computed exactly through over-integration by product rules based on Legendre Gauss quadratures [52].

A final key operation needed for the implementation of the scheme is surface integration, i.e.,

$$(f_N, g_N)_{\delta\mathsf{D}} = \oint_{\delta\mathsf{I}} f_N(\boldsymbol{\xi}) g_N(\boldsymbol{\xi}) J(\boldsymbol{\xi})\, d\boldsymbol{\xi} \quad ,$$

where $J(\boldsymbol{\xi})$ refers to the surface Jacobian only. While one could proceed as for the volume integral discussed above, it is more natural to exploit the uniqueness and completeness of the Lagrange interpolation. To illustrate the procedure, let us restrict attention to one of the faces, face 'd' (see Fig. 1), and term those $N_n^{\mathrm{d}} = \frac{1}{2}(n+1)(n+2)$ nodes positioned at that face for $\boldsymbol{\xi}^{\mathrm{d}}$. Clearly, using the exact same procedure as for the three-dimensional Lagrange polynomial discussed above, we can compute a two-dimensional Lagrange polynomial, $l_j^{\mathrm{d}}(\xi, \eta)$ based on $\boldsymbol{\xi}^{\mathrm{d}}$. As for $L_j(\boldsymbol{\xi})$, we can recover l_j^{d} as the solution to the dual problem

$$\left(\mathrm{V}^{\mathrm{d}}\right)^T \boldsymbol{l}^{\mathrm{d}} = \boldsymbol{p}^{\mathrm{d}} \quad ,$$

where the entries of the Vandermonde matrix is

$$\mathrm{V}_{ij}^{\mathrm{d}} = p_j^{\mathrm{d}}(\boldsymbol{\xi}_i^{\mathrm{d}}) \quad .$$

The proper basis to use is the two-dimensional version of Eq.(32) given directly as $p_j^{\mathrm{d}}(\xi, \eta) = \psi_{ij0}(\xi, \eta, -1)$. This allows us to proceed exactly as for the volume integration and express the integration over face 'd' as

$$\int_{\text{face d}} f_N(\xi, \eta, -1) g_N(\xi, \eta, -1) J(\xi, \eta, -1)\, d\xi\, d\eta = \left(\left(\mathrm{V}^{\mathrm{d}}\right)^{-1} \boldsymbol{f}^{\mathrm{d}}\right)^T \mathrm{W}^{\mathrm{d}} \left(\mathrm{V}^{\mathrm{d}}\right)^{-1} \boldsymbol{g}^{\mathrm{d}} \quad ,$$

where $\boldsymbol{f}^{\mathrm{d}} = [f_N(\boldsymbol{\xi}_0^{\mathrm{d}}), ..., f_N(\boldsymbol{\xi}_{N_n^{\mathrm{d}}}^{\mathrm{d}})]^T$ is the trace of f_N at the face. A similar definition is used for $\boldsymbol{g}^{\mathrm{d}}$. The matrix of surface weights are given as

$$\mathrm{W}_{ij}^{\mathrm{d}} = \int_{\text{face d}} \psi_i(\xi, \eta, -1) \psi_j(\xi, \eta, -1) J(\xi, \eta, -1)\, d\xi d\eta \quad .$$

In the important special case where the face is planar and has straight edges, orthonormality of the polynomials immediately implies that $\mathrm{W}^{\mathrm{d}} = J^{\mathrm{d}}\mathrm{I}$ as for the volume case. For the general case we shall use a cubature rule [53, 54, 55] of sufficiently high order to evaluate the inner product, i.e., we need to interpolate the polynomials, f_N and g_N, onto the M cubature nodes, $\boldsymbol{\xi}^{\mathrm{d,cub}}$, situated at the face. This is done by the introduction of the interpolation operator

$$\mathrm{H} = \mathrm{P}^T \left(\mathrm{V}^{\mathrm{d}}\right)^{-1} \quad , \quad \mathrm{P}_{ij} = p_i^{\mathrm{d}}(\boldsymbol{\xi}_j^{\mathrm{d,cub}}) \quad ,$$

i.e., P is an $N^{\mathrm{d}} \times M$ operator. The evaluation of the inner product is then accomplished as

$$\int_{\text{face d}} f_N(\xi,\eta,-1) g_N(\xi,\eta,-1) J(\xi,\eta,-1)\, d\xi\, d\eta = \left(\boldsymbol{f}^{\mathrm{d}}\right)^T \mathrm{H}^T \mathrm{W} \mathrm{H} \boldsymbol{g}^{\mathrm{d}} \quad ,$$

where the entries of the diagonal $M \times M$ matrix of weights are given as

$$\mathrm{W}_{ii} = w_i \sum_{k=0}^{N_n^{\mathrm{d}}} \mathrm{H}_{ik}\, J(\boldsymbol{\xi}_k^{\mathrm{d}}) \quad ,$$

containing the weights w_i of the cubature as well as the interpolation of the transformation Jacobian of the curvilinear face. While this formulation leads to the most compact scheme it proves advantageous to operate directly on the values at the cubature nodes as they do not include the edges and vertices, i.e., we can establish a clean face based connection between elements without considering the multiplicity of solutions at vertices and the added complexity this introduces for the implementation and performance. Needless to say, the whole discussion for the evaluation of the integral over face 'd' carries over directly to the other faces, hence completing the evaluation of the full surface integral.

It is important to realize that all the operators introduced in the above can be initialized during a preprocessing phase. Furthermore, it is worth recalling the discussion in Sec. 3.1 in which we found that any two straightfaced tetrahedra are connected through a linear transformation. Hence, for any straightfaced D we can form any of the operators discussed in the above directly by a linear scaling of hard-coded template operators defined on I. This saves not only preprocessing time but also reduces the required storage space very substantially.

REFERENCES

[1] H. O. Kreiss and J. Oliger, *Comparison of Accurate Methods for the Integration of Hyperbolic Problems*, Tellus **24**(1972), pp. 199-215.

[2] A. T. Patera, *A Spectral Element Method for Fluid Mechanics: Laminar Flow in a Channel Expansion*, J. Comput. Phys. **54**(1984), pp. 468-488.

[3] K. Z. Korczak and A. T. Patera, *An Isoparametric Spectral Element Method for Solution of the Navier-Stokes Equations in Complex Geometries*, J. Comput. Phys. **62**(1986), pp. 361-382.

[4] C. Canuto, M. Y. Hussaini, A. Quarteroni, and T. A. Zang, *Spectral Methods in Fluid Dynamics*. Springer Series in Computational Physics. Springer-Verlag. New York, 1988.

[5] D. A. Kopriva, *A Spectral Multidomain Method for the Solution of Hyperbolic Systems*, Appl. Numer. Math. **2**(1986), pp. 221-241.

[6] D. A. Kopriva, *Computation of Hyperbolic Equations on Complicated Domains with Patched and Overset Chebyshev Grids*, SIAM J. Sci. Stat. Comput. **10**(1989), pp. 120-132.

[7] A. Quarteroni, *Domain Decomposition Methods for Systems of Conservation Laws: Spectral Collocation Approximations*, SIAM J. Sci. Stat. Comput. **11**(1990), pp. 1029-1052.

[8] D. A. Kopriva, *Multidomain Spectral Solution of the Euler Gas-Dynamics Equations*, J. Comput. Phys. **96**(1991), pp. 428-450.

[9] J. G. Giannakouros and G. E. Karniadakis, *Spectral Element-FCT Method for the Compressible Euler Equations*, J. Comput. Phys. **115**(1994), pp. 65-85.

[10] J. S. Hesthaven, *A Stable Penalty Method for the Compressible Navier-Stokes Equations: III. Multidimensional Domain Decomposition Schemes*, SIAM J. Sci. Comput. **20**(1999), pp. 62-93.

[11] B. Yang, D. Gottlieb, and J. S. Hesthaven, *Spectral Simulations of Electromagnetic Wave Scattering*, J. Comput. Phys. **134**(1997), pp. 216-230.

[12] B. Yang and J. S. Hesthaven, *A Pseudospectral Method for Time-Domain Computation of Electromagnetic Scattering by Bodies of Revolution*, IEEE Trans. Antennas Propaga. **47**(1999), pp. 132-141.

[13] J. S. Hesthaven, P. G. Dinesen, and J. P. Lynov, *Spectral Collocation Time-Domain Modeling of Diffractive Optical Elements*, J. Comput. Phys. **155**(1999), pp. 287-306.

[14] D. A. Kopriva, S. L. Woodruff, and M. Y. Hussaini, *Discontinuous Spectral Element Approximation of Maxwell's Equations*. In Discontinuous Galerkin Methods: Theory, Computation and Applications. B. Cockburn, G. E. Karniadakis, and C.W. Shu (Eds). Lecture Notes in Computational Science and Engineering **11**(2000), Springer Verlag, New York. pp. 355-362.

[15] B. Yang and J. S. Hesthaven, *Multidomain Pseudospectral Computation of Maxwells Equations in 3-D General Curvilinear Coordinates*, Appl. Numer. Math. **33**(2000), pp. 281-289.

[16] S. J. Sherwin and G. E. Karniadakis, *A New Triangular and Tetrahedral Basis for High-Order Finite Element Methods*, Int. J. Num. Meth. Eng. **38**(1995), pp. 3775-3802.

[17] S. J. Sherwin and G. E. Karniadakis, *Tetrahedral hp Finite Elements: Algorithms and Flow Simulations*, J. Comput. Phys. **124**(1996), pp. 14-45.

[18] I. Lomtev, C. B. Quillen and G. E. Karniadakis, *Spectral/hp Methods for Viscous Compressible Flows on Unstructured 2D Meshes*, J. Comput. Phys. **144**(1998), pp. 325-357.

[19] T. Warburton and G. E. Karniadakis, *A Discontinuous Galerkin Method for the Viscous MHD Equations*, J. Comput. Phys, **152**(1999), pp. 608-641.

[20] T. Warburton, I. Lomtev, Y. Du, S. Sherwin, and G. E. Karniadakis, *Galerkin and Discontinuous Galerkin Spectral/hp Methods*, Comput. Methods Appl. Mech. Engrg. **175**(1999), pp. 343-359.

[21] G. E. Karniadakis and S. J. Sherwin, *Spectral/hp Element Methods for CFD*. Numerical Mathematics and Scientific Computation. Clarendon Press, Oxford, 1999.

[22] H. Atkins and C.W. Shu, *Quadrature-Free Implementation of Discontinuous Galerkin Methods for Hyperbolic Equations*, AIAA J. **36**(1998), pp. 775-782.

[23] B. Cockburn, G. E. Karniadakis, and C.-W. Shu (Eds.), *Discontinuous Galerkin Methods: Theory, Computation and Applications*. Lecture Notes in Computational Science and Engineering **11**, Springer Verlag, New York, 2000.

[24] I. Babuška and M. Suri, *The hp-Version of the Finite Element Method with Quasiuniform Meshes*, M^2AN, **21**(1987), pp. 199-238.

[25] C. Schwab, *p- and hp-Finite Element Methods. Theory and Applications in Solid and Fluid Mechanics*. Numerical Mathematics and Scientific Computation. Clarendon Press, Oxford, 1998.

[26] J. S. Hesthaven, *Spectral Penalty Methods*, Appl. Numer. Math. **33**(2000), pp. 23-41.

[27] M. H. Carpenter and D. Gottlieb, *Spectral Methods on Arbitrary Grids*, J. Comput. Phys.

129(1996), pp. 74-86.

[28] J. S. Hesthaven and D. Gottlieb, *Stable Spectral Methods for Conservation Laws on Triangles with Unstructured Grids*, Comput. Methods Appl. Mech. Engin. **175**(1999), pp. 361-381.

[29] J. S. Hesthaven and C. H. Teng, *Stable Spectral Methods on Tetrahedral Elements*, SIAM J. Sci. Comput. **21**(2000), pp. 2352-2380.

[30] T. Warburton and J. S. Hesthaven, *High-Order/Spectral Methods on Unstructured Grids. II. General Systems of Conservation Laws*, J. Comput. Phys. – submitted.

[31] Q. Chen and I. Babuška, *The Optimal Symmetrical Points for Polynomial Interpolation of Real Functions in a Tetrahedron*, Comput. Methods Appl. Mech. Engrg. **137**(1996), pp. 89-94.

[32] A. H. Mohammadian, V. Shankar, and W. F. Hall, *Computation of Electromagnetic Scattering and Radiation using a Time-Domain Finite-Volume Discretization Procedure*, Comput. Phys. Comm. **68**(1991), pp. 175-196.

[33] I. Babuška and A. K. Aziz, *On the Angle Condition in the Finite Element Method*, SIAM J. Numer. Anal. **13**(1976), pp. 214-226.

[34] A. Ditkowski, *Bounded-Error Finite Difference Schemes for Initial Boundary Value Problems on Complex Domains*. PhD-Thesis, Department of Applied Mathematics, School of Mathematical Sciences, Tel-Aviv University, Tel-Aviv, Israel. 1997.

[35] E. Suli, C. Schwab, and P. Houston, *hp-DGFEM for Partial Differential Equations with Nonnegative Characteristic Form*. In "Discontinuous Galerkin Methods. Theory, Computation and Applications", B. Cockburn, G. E. Karniadakis, and C. W. Shu (Eds). Lecture Notes in Computational Science and Engineering **11**, Springer Verlag, Berlin, pp. 221-230.

[36] M. H. Carpenter and C. A. Kennedy, *Fourth order 2N-storage Runge-Kutta scheme*, NASA-TM-109112, NASA Langley Research Center, VA. 1994.

[37] S. Abarbanel and D. Gottlieb, *On the Construction and Analysis of Absorbing Layers in CEM*, Appl. Numer. Math. **27**(1998), pp. 331-340.

[38] A. Taflove, *Computational Electrodynamics: The Finite-Difference Time-Domain Method*. Artech House, Boston, 1995.

[39] J. J. Bowman, T. B. A. Senior, and P. L. Ushlenghi (Eds.), *Electromagnetic and Acoustic Scattering by Simple Shapes*. North-Holland, Amsterdam, 1969.

[40] P. W. Barber and S. C. Hill, *Light Scattering by Particles: Computational Methods*. World Scientific Publishing Company, Singapore, 1990.

[41] J. L. Volakis, *Benchmark Plate Radar Targets for the Validation of Computational Electromagnetics Programs*, IEEE Antennas Propagat. Mag. **34**(1992), pp. 52-56.

[42] J. Dongarra, J. Du Croz, I. Duff, and S. Hammerling, *A Set of Level 3 Basic Linear Algebra Subprograms (BLAS)*, http://www.netlib.org/blas/blas3-paper.ps

[43] M. Snir, S. Otto, S. Huss-Lederman, D. Walker, and J. Dongarra, *MPI: The Complete Reference*. MIT Press, 1996.

[44] G. Karypis and V. Kumar, *Multilevel k-way Partitioning Scheme for Irregular Graphs*, J. Paral. Distrib. Comput. **48**(1998), pp. 96-129.

[45] Y. Saad, *Iterative Methods for Sparse Linear Systems*. 2nd Edition, 2000. http://www-users.cs.umn.edu/ ∼saad/books.html

[46] C. C. Douglas, G. Haase, J. Hu, M. Kowarschik, U. Rüde, and C. Weiss, *Portable Memory Hierarchy Techniques for PDE Solvers: Part II*. SIAM News **33**(2000).

[47] R. Biswas, K. D. Devine, and J. Flaherty, *Parallel, Adaptive Finite Element Methods for Conservation Laws*, Appl. Numer. Math. **14**(1994), pp. 255-283.

[48] J. Proriol, *Sur une Famille de Polynomes à deux Variables Orthogonaux dans un Triangle*, C. R. Acad. Sci. Paris **257**(1957), pp. 2459-2461.

[49] T. Koornwinder, *Two-variable Analogues of the Classical Orthogonal Polynomials* in "Theory and Application of Special Functions", R. A. Askey ed., Academic Press, 1975, pp. 435-495.

[50] M. Dubiner, *Spectral Methods on Triangles and Other Domains*, J. Sci. Comput. **6**(1991), pp. 345-390.

[51] G. Szegö, *Orthogonal Polynomials.* Colloquium Publications **23**, American Mathematical Society, Providence, RI, 1939.

[52] P. J. Davis and P. Rabinowitz, *Methods of Numerical Integration.* Computer Science and Applied Mathematics, Academic Press, New York, 1975.

[53] A. H. Stroud, *Approximate Calculation of Multiple Integrals.* Prentice-Hall Publishing, New Jersey, 1971.

[54] R. Cools and P. Rabinowitz, *Monomial cubature rules since Stroud: A Compilation* J. Comput. Appl. Math. **48**(1993), pp. 309-326.

[55] R. Cools, *Monomial cubature rules since Stroud: A Compilation - Part 2* J. Comput. Appl. Math. **112**(1999), pp. 21–27.